# COUPLED FLUID-CHEMICAL COMPUTATIONAL MODELING OF ANTICOAGULATION THERAPIES IN A STENTED ARTERY

by

Anirban Ghosh

A thesis submitted to Johns Hopkins University in conformity with the requirements for the degree of Master of Science in Engineering

Baltimore, Maryland

May, 2014

# Abstract

Stent thrombosis is a major complication that occurs after the placement of stents in the coronary artery through balloon angioplasty, associated with severe medical conditions with a high risk of mortality. The common treatment for stent thrombosis is to provide patients with anticoagulant and antiplatelet therapy through the bloodstream, which has the adverse effect of increased risk of bleeding disorders. This study uses numerical modeling to compare two delivery methods of anticoagulant to the arterial wall to reduce thrombus formation: through the flow and via a drug-eluting stent. A two-dimensional thrombosis model is developed that couples an incompressible flow solver with a convection-diffusion-reaction equation model of the coagulation cascade and platelet activation and aggregation. The results find that the drug-eluting stent delivery of anticoagulant is more effective in reducing platelet activation and clotting, while also providing a more localized anticoagulant distribution.

# Acknowledgements

I would like to sincerely thank my advisor, Professor Rajat Mittal, for granting me the opportunity to work with him for these past two years. I have learned a tremendous amount under his mentorship that will continue to help me as I continue ahead on my career path. It has been a privilege to work with him and I could not have completed this essay without his guidance, support, and encouragement. I would also like to thank Professor Tamer Zaki for reading this thesis and for his encouraging words.

I would also like to thank Dr. Jung-Hee Seo for working with me on this project and providing vital advice and assistance through this project. I am grateful too for the help and support of all of my lab members in the Flow Physics and Computation Laboratory on this and other projects.

Finally, I would like to thank my family for their endless love and support throughout this process. My father has stood beside me at every step of my academic and professional experiences to provide me with invaluable advice, encouragement, and inspiration, and my mother and grandmother have cared for me and supported me through my journey. They have always been there for me through the good and the bad, and I would not be here today if it were not for their presence throughout my life.

# Table of Contents

# List of Tables

# List of Figures

# 1 Introduction

Blood flow in the human body is regulated by a variety of physical and chemical processes. In the event of injury to vascular tissue in the body, there is a complex set of responses known as hemostasis that is used to maintain the integrity of the tissue wall and blood flows. The first response to such tissue damage is to plug the injured area with an aggregated mass of platelets. This process of blood clotting is known as thrombus formation.

There exist a multitude of different biochemical, biophysical, and biomechanical mechanisms that govern platelet activity and thrombus formation. When working properly the set of processes produces a blood clot localized at the site of the injury, which acts to stop hemorrhage as the blood vessel heals. These processes are initiated by certain chemical agents released from the injured tissue wall, and also by the mechanical conditions to which the platelets are subjected.

However, thrombus formation can sometimes occur in arteries and veins when pathologic processes interfere with the natural mechanisms of hemostasis, creating unnecessary clots that can obstruct normal blood flow. This event, known as thrombosis, is the cause of cardiovascular conditions such as myocardial infarction, stroke, and pulmonary embolism which are some of the leading causes of morbidity and mortality in the world.

Timely and accurate detection of thrombosis is vital for effective treatment, and the development of a patient-specific thrombus formation model would be a powerful tool in the prediction of thrombosis in blood flows. This work in this essay is purposed towards developing and applying such a computational model to study the effect of anti-thrombotic therapy in patients with stents.

## 1.1 Overview of Thrombosis

### 1.1.1 Platelet Characteristics

**Figure 1:** From left to right, scanning electron microscope images of resting, partially activated, and fully activated human platelets. [**21**]

Platelets, or thrombocytes, are non-nucleated cells that are created by bone marrow megakaryocytes and released into the bloodstream, where they circulate freely. Typical platelet count is about 150-350 × $10^9$ $L^{-1}$, which forms about three percent of all particulate matter in human blood. [**1**] The lifespan of a platelet is 8-10 days, and in total the human body contains about one trillion platelets, of which 1 × $10^{11}$ are produced daily. [**19**] [**21**] In their resting form they are smooth and discoid in shape with a cell diameter of 1-2 µm and a volume of approximately 6 µ$m^3$. [**1**] [**19**]

Platelets are used to block hemorrhage after vascular tissue injury, and this is done through the process of activation. The outermost glycoprotein layer of the platelets, or glycocalyx, contains receptors for activating factors (e.g. collagen-bound von Willebrand factor, thrombin, or ADP) as well as for inhibitors, adhesive agents, and aggregating agents. [**1**] [**13**] When the platelet is activated, it changes shape from a flattened discoid into a spheroid, and extends many pseudopods to interact with other activated platelets. [**19**] Figure 1 illustrates this shape change between resting and activated platelets.

### 1.1.2 Platelet Activation, Adhesion, and Aggregation

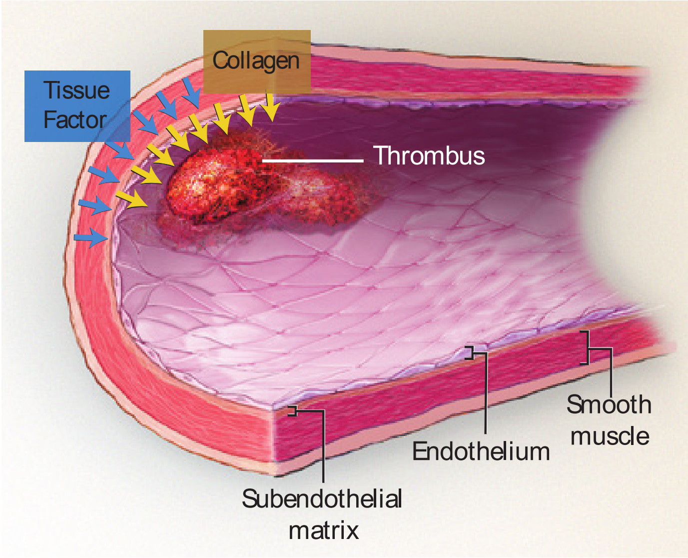

**Figure 2:** Thrombus formation as a typical response to vascular tissue injury. [**13**]

To produce a thrombus as a response to damaged vascular tissue, typically three separate processes must occur. First, platelets must be activated through chemical pathways. These activated platelets must then bind locally to the endothelial wall of the injured vessel. Simultaneously, they must also attach to other activated platelets to create an aggregate that effectively plugs the damaged area and prevents hemorrhage as it heals. Figure 2 depicts characteristic thrombus development following this process.

## Platelet Activation

The plasma membrane of the platelet contains receptors for several different biochemical factors, each with their own unique signaling pathways that are effected by enzymatic reactions. As a result, there exist various chemicals and signaling factors that can activate a platelet. Activation can be stimulated by any of the following biomolecules: von Willebrand factor (vWF), collagen, thrombin, thromboxane, serotonin, adenosine diphosphate (ADP), or epinephrine binding to their own specific receptors on the platelet membrane. [**13**] [**21**]

There are two distinct pathways that are naturally used by the body to trigger activation. Platelets are activated in response to blood vessel tissue injury, so the first mechanism is by the exposure of platelets to subendothelial collagen in the tissue. Collagen is a matrix protein found in most body tissues, with its primary role being structural. Collagen itself can interact with platelet glycoprotein VI on the membrane, and collagen-bound von Willebrand factor also can bind with platelet glycoprotein Ib-V-IX to initiate activation. [**13**] Eventually this signaling pathway activates platelet integrin and leads to adhesion to the vessel wall. [**14**]

The second pathway is separately initiated by an agent known as tissue factor (TF). Tissue factor normally resides in the endothelium and is only exposed to the bloodstream when the vessel wall is ruptured, exposing the subendothelial tissue. Upon contact with blood, tissue factor binds with factor VII that flows through the bloodstream to form the complex TF:VIIa. [**4**] [**13**] [**14**] This sets into motion the coagulation cascade (CC), a series of enzyme reactions in the bloodstream that are ultimately responsible for the production of thrombin. Through a platelet surface reaction, thrombin cleaves a protease-activated receptor to activate the platelet. [**13**]

After the completion of either pathway, the activated platelet itself becomes a source for chemical agonists. Active platelets release thromboxane $A_2$, ADP, and serotonin into the nearby blood, all of which are potential activators for additional platelets through surface membrane chemical reactions. [**8**] [**13**]

## Platelet Adhesion

Activated platelets bind to the injured cell wall through the process of adhesion. Healthy endothelial cells produce the glycoprotein von Willebrand factor and secrete it into the subendothelial matrix, where some of it also binds to the collagen in the matrix. [**19**] If the vessel wall is ruptured then von Willebrand factor and collagen are exposed to activated platelets in the bloodstream. Von Willebrand factor binds to the glycoprotein (GP) IIb/IIIa and GP Ib-V-IX complexes on the membrane of the extended pseudopods of the activated platelet, while collagen binds with GP VI. The collagen-GP VI link is required for binding the platelet to the exposed subendothelium. [**13**]

Since adhesion is a process that connects free flowing platelets from the bloodstream to the relatively stationary wall, the links must be able to withstand the forces induced by the flow of blood. The importance of the different links is determined by the local wall shear rates and stresses. Higher shear rates limit the time of contact between platelets and the vessel wall and thus the amount of wall binding is reduced. In the event of high shear rates, only the vWF link with GP Ib-V-IX occurs quickly enough to effectively snag platelets from the blood. However for lower shear rates the process can occur even without the presence of vWF. Relatedly, higher shear stresses reduce the lifetime of established platelet links and make it easier for adhered platelets to detach from the wall. [**13**] [**19**] [**33**]

## Platelet Aggregation

The platelets bound to the subendothelial wall also attach themselves to other activated platelets, leading to the formation and growth of a clot. This process is known as aggregation. It is related to adhesion in that many of the same adhesive ligand and receptor pairs are used, only they attach to the membranes of wall-bound platelets instead of the matrix and tissues of the vascular wall. [**32**] Specifically, the complexes GpIb and GpIIb-IIIa are used as receptors for von Willebrand factor and fibrinogen/fibrin protein links between platelets. [**1**] [**19**] As with adhesion, platelet aggregation is adversely impacted by high shear stresses. [**1**]

Concurrently to the formation of platelet-platelet links, a fibrin matrix is assembled at the location of the clot. Fibrinogen is converted to fibrin monomers called protofibrils through the action of thrombin from the coagulation cascade. [**1**] The protofibrils branch and form a three-dimensional matrix around and through the clot. They are cross-linked together via Factor XIII, a blood-borne transglutaminase that is activated by thrombin. As platelets attach to this growing fibrin matrix the clot grows in size. The fibrin matrix offers the bound platelets protection from both mechanical stresses and chemical breakdown, and the resulting platelet-fibrin structure represents the end product of thrombus formation. [**5**] [**19**]

Clot dissolution after the tissue has healed is characterized by the process of fibrinolysis. Fibrinolysis is triggered by the release of tissue PLS activator (tPA) and urokinase-like PLS activator (uPA) from endothelial cells through the action of thrombin and fibrin. Since these activators are secreted from healthy endothelial cells, this process occurs after the vascular tissue has healed and an intact endothelium has formed over the previously injured area. These chemicals transform PLS into the enzyme plasmin, which acts to break up the fibrin matrix. After this, various inhibitory factors act on the remaining elements of the clot and coagulation cascade to restore hemostatic conditions. [**1**] [**5**]

### 1.1.3 The Coagulation Cascade and Clot Formation

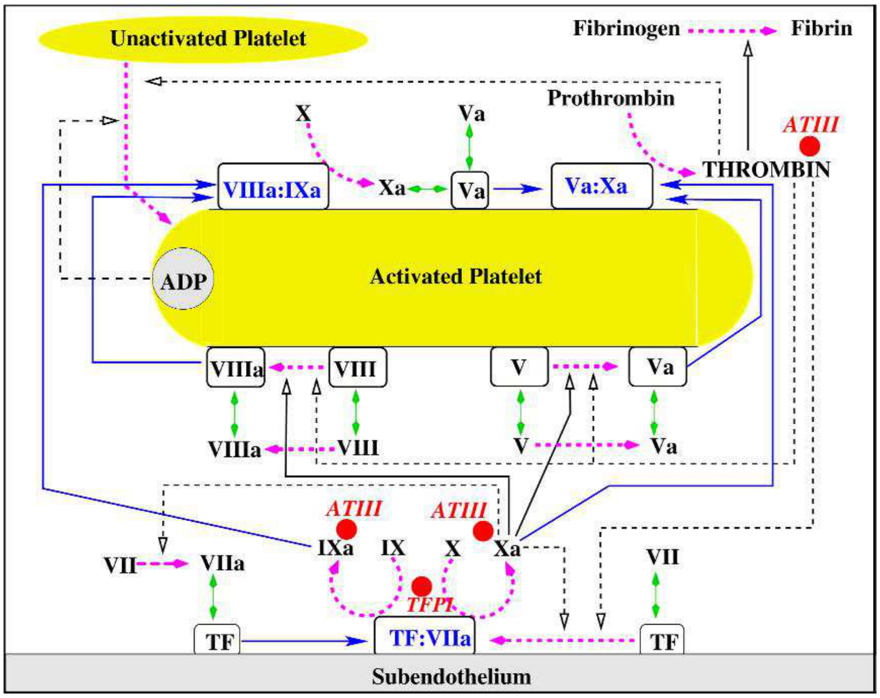

**Figure 3:** A schematic of the coagulation cascade including species and reactions. The dashed magenta arrows represent activation processes, blue arrows represent chemical transport, green segments represent surface binding/unbinding, solid black lines represent forward enzyme action, dashed black lines show enzyme feedback, and red disks represent chemical inhibitors. [**22**]

The coagulation cascade refers to a series of reactions with the net result of producing thrombin and ultimately fibrin. The term cascade refers to the amplification property of the reactions: small amounts of initial chemicals are used activate much larger quantities of later enzymes and products. Injury to the vessel wall initiates this process, which supplies the additional chemicals that are needed to take free, mobile platelets from the blood, activate them, and form a clot local to the site of the injury. The various chemical reactions take place on the subendothelium and platelet surfaces as well as in the free stream of the blood. [**5**] The coagulation cascade contains a main extrinsic pathway, as well as an intrinsic pathway characterized by contact activation. [**1**] [**4**] [**12**] Figure 3 shows the many different reactions and agents of the coagulation cascade.

For the extrinsic pathway, coagulation is initiated by the release of tissue factor, a membrane protein normally found in different cellular compartments. When not used in the coagulation cascade it can also play a role in cellular signaling events for angiogenesis, tumor progression, metastasis, and yolk-sac vasculature maintenance. While latent tissue factor does exist in the bloodstream, coagulation is started when the active form is released through injury to the endothelium and reacts with factor VIIa in the blood. [**13**] Together they form factor TF:VIIa on the subendothelium as the first step in the coagulation cascade. After this, various proenzymes, or zymogens, are converted to their active enzyme states as the cascade progresses. [**1**] Tissue factor is also involved in positive feedback, as endothelium and activated platelets may also produce protein disulfide isomerase, which converts latent tissue factor to its active form.

The common result of both the extrinsic and intrinsic coagulation pathways is the production of thrombin. As mentioned before, thrombin serves to activate platelets as well as form from fibrinogen the fibrin monomers that make up the blood clot. Thrombin also has a large role in feedback mechanisms for coagulation. It activates coagulation reaction factors XI, V, and VIII to effect the cascade, but it also catalyzes the formation of anticoagulant active protein C (APC). [**1**] [**5**]

There exist three main chemical inhibitors for the coagulation cascade. The most important of these is Antithrombin III (ATIII). ATIII directly inhibits thrombin in a 1:1

ratio by binding to it, and it also binds to and deactivates factors Xa, XIIa, IXa, and XIa. It also has an inhibitory effect on the subendothelium-bound TF:VIIa complex. [**5**] ATIII is found in the blood at much higher concentrations than any of the coagulation zymogens, and its activity is also significantly increased by sulfated heparin that is produced and released from endothelial cells. [**1**] Another chemical, tissue factor pathway inhibitor (TFPI), binds with factor Xa catalyzed by the TF:VIIa complex. TFPI is produced mainly in endothelial cells and its actions effectively disable the extrinsic pathway. APC is the third main inhibitor, and it deactivates factors Va and VIIa. [**1**] [**4**] [**5**] [**12**]

Mechanical factors can also affect the coagulation reactions since these have an effect on platelet adhesion and aggregation. As various steps in the coagulation cascade take place on the surface of the platelets, the availability of binding sites is affected by the shear stresses in the blood. This is particularly true for the assembly of cascade intermediates tenase and prothrombinase. Experiments also suggest that fibrin formation is related to shear rates, and that fibrin can form even in areas with intact endothelium, most noticeably in recirculation zones. [**1**]

## 1.2 Thrombosis in Selected Blood Flows

When functioning properly, the aforementioned pathways help regulate concentrations of various chemicals as needed for hemostasis and allow vascular tissue to safely recover from injury. However, unwanted occurrences of thrombosis can produce significant medical problems. A blood clot is capable of partially or even fully blocking a blood vessel. This leads to ischemia, or oxygen deprivation and tissue starvation downstream of the blockage. [**5**] Ischemia can result in tissue damage or death, which can be hazardous or even fatal for key organs of the body such as the heart or brain in myocardial infarction or stroke. [**28**] Also, if the clot is detached from its original location due to blood shear stresses, it can migrate through the bloodstream and affect faraway tissues as well. This is known as downstream embolization. [**1**]

Thrombosis-related disorders that develop in the heart have a high risk associated with them. Atrial thrombosis can occur as a consequence of arrhythmia such as atrial fibrillation or atrial flutter. The impaired contraction of the atrium lowers the diastolic flow volume and speed of blood into the ventricle, leading to formation of a thrombus in the atrium. [**1**] Ventricular thrombosis is normally less likely than atrial thrombosis, but is often caused by local systolic dysfunction of the ventricle. For example, the incidence of left ventricular thrombosis (LVT) is high after myocardial infarction (MI) or severe apical wall abnormality. [**2**] [**39**] Systolic volume of the ventricle appears to play a role in the development of LVT. [**30**] Incidence of thrombosis on the heart valves themselves is naturally very rare, but thrombi do form more frequently on artificial mechanical valves. [**1**]

Arterial and venous thrombosis occurs after the formation of an atherosclerotic plaque in a blood vessel, a slow process that can take many years. After its development, the plaque could go unstable and rupture, which triggers thrombosis. Thrombosis in the artery or vein causes stenosis, and a large enough clot leads to ischemia and its associated negative effects. [**1**] [**5**] Thrombosis also often occurs in aneurysms in vascular tissue, where the extracellular matrix has been irreversibly remodeled causing a loss of structural integrity in the vessel wall. An Intra-Luminal Thrombus (ILT) tissue forms and causes localized hypoxia and wall thinning and weakening. This could eventually lead to a rupture, and for an aneurysm in the aorta, brain, or other important organs, the effect is likely to be fatal. [**4**] [**29**] Thrombosis can also occur in the veins of the lungs, which can migrate to the ventricle and become a pulmonary embolism. [**21**] It is also believed that inflammation and thrombosis are inherently linked; inflammation can initiate local thrombosis, and thrombosis can amplify inflammation. [**8**] [**23**]

These thrombosis-related complications in the body are often linked to local blood flow properties. It is widely believed that local flow stagnation can induce thrombosis. Atrial thrombosis is caused by atrial arrhythmia, which affects the atrial blood flow considerably. [**1**] Abnormal flow as measured by Doppler echocardiography is considered one of the largest risk factors for the formation of LVT. [**30**] [**39**] Unstable atherosclerotic plaques in blood vessels often lead to regions of stenosis where flow instability and stagnation can be observed. [**1**] In aneurysms a strong correlation is observed between the locations of thrombi and low shear stresses and flow velocities. [**4**] [**32**] Pulmonary thrombus also occurs in the low flow venous circuit of the lungs. [**21**] It is clear that flow stagnation and abnormal flow are correlated to the location of thrombus formation.

Various options are currently used to prevent and treat thrombosis-related complications. The most common treatment is anticoagulants such as heparin and warfarin that interfere with the coagulation cascade. Antiplatelet therapy, often used in arterial thrombosis, may also be used to prevent platelet aggregation. These can be given through intravenous injections, subcutaneous injections, or oral methods. However, both of these treatments contain a substantial early and late risk of bleeding complications. [**1**] Drugs to induce thrombolysis have shown limited ability to treat thrombosis, as the likelihood of embolism becomes high. In certain cases such as large thrombi or particularly dangerous embolisms, surgery is also used to physically remove the clot. [**39**]

## 1.3 Modeling of Thrombosis

Because of the risks of many thrombosis-related disorders, there is a large demand for predictive models. However, taking into account the various chemicals and reactions involved, the distinct pathways for thrombosis such as platelet activation, and the relative importance of different factors presents a significant challenge in model development. Over the past few decades there has been significant work in this field, resulting in a large variety of models for thrombogenesis. Some common categories will be described here.

Wall shear stress models use the correlation between local wall shear stress and platelet adhesion and aggregation. For subendothelium and collagen surfaces, platelet adhesion and aggregation have been observed to increase directly with shear rate. Areas of low wall shear stress are also predicted to give prolonged surface contact time and are associated with endothelial expression of various adhesive molecules. [**24**]

Platelet-binding models focus on the chemical and mechanical links that form in platelet adhesion and aggregation. Guy (2002) develops a mathematical model that uses collision dynamics and assumptions about platelet receptor occupancy to determine the capture probability, indicating whether two activated platelets will form a fibrinogen bond. The newly-formed bond must be strong enough to overcome hydrodynamic forces that act to separate the platelets. [**15**] Mori (2008) uses a computational model to simulate platelet adhesion and aggregation in the presence of von Willebrand factor and fibrinogen. The particle binding was modeled as spring forces using the Voigt model, and hydrodynamic forces were calculated from Stokesian dynamics. [**28**]

Many models of thrombosis are geared towards determining the locations and likelihood of thrombus formation, and so they may use simplified models in order to produce a metric for thrombotic risk. Residence time models fall under this category. Flow residence time, broadly defined, is an indicator of how long a particle in a flow will remain close to its original location. Longest (2003) uses Lagrangian dynamics to introduce a near-wall residence time (NWRT) parameter calculated from flow velocities and particle dynamics, and demonstrates agreement with experimental data. The NWRT model also significantly outperforms the wall shear stress models used for comparison as well. [**24**] Residence time has also been modeled as a scalar that is transported by the flow via passive diffusion. A simplified residence time model of this kind was proposed by Narracott (2005) for determining thrombus formation risk in aneurysms. [**29**] Harrison (2007) combines a residence time scalar transport approach with the Lattice-Boltzmann method to provide a model that can be solved in complex and changing geometries. [**16**] Rayz (2010) simulated advection of a “virtual ink” in flow in a patient-specific aneurysm and found that thrombi are most likely to form in areas of high residence time and low wall shear stress. [**32**]

Some of the more complex thrombosis models can be split up into Lagrangian and Eulerian models. Lagrangian models rely on particle tracking or numerical methods such as the Lattice Boltzmann method to solve the equations for platelet adhesion and aggregation. Harrison's residence time model mentioned above also fits in this category. Filipovic (2008) uses the Discrete Particle Dynamics (DPD) algorithm to model interactions between blood plasma, platelets, and the vessel wall through adhesion and aggregation in a simple parallel plate shear flow. The conservative, dissipative, and random forces acting on the platelets are characterized by effective spring constants found from matching to experimental data. [**10**] Tamagawa (2009) developed a Lattice-Boltzmann model to directly model the influence of shear rate on fibrinogen aggregation in a backward facing step flow. The activated fibrinogen is subject to higher surface tension forces to measure aggregation; platelets are not directly considered in this model. [**37**] The moving particle semi-implicit (MPS) method was used by Kamada (2010) to model three-dimensional thrombogenesis in a rectangular channel at low Reynolds number, again using a spring force to model adhesion and aggregation of platelets. The model investigated the formation and collapse of thrombus, including feedback reactions of thrombus development and flow. [**18**]

Eulerian models of thrombus development typically use a set of coupled advection-diffusion equations to model the reactions between different chemical species. Sorensen (1999) simulates platelet adhesion and aggregation with agonist release and reactions to produce a model of platelet activation and deposition in flowing blood. The model uses a finite volume code and a coupled set of reactions for resting and activated platelets, agonists, thrombin, antithrombin, and other factors. [**35**] [**36**] Wootten (2001) uses computational fluid dynamics, species transport, and a kinetic model of platelet activation and aggregation to model thrombosis over an atherosclerotic plaque. [**42**] Anand (2003) employed a finite difference code for the flow and solved coupled nonlinear transport equations for the coagulation cascade, fibrin production, and thrombosis inhibitors. The thrombus was modeled as a highly viscous fluid and clot formation and dissolution could be simulated. [**1**] Leiderman (2011) modeled activation, adhesion, and aggregation as reactions between different species of platelets. These reactions were coupled with the flow solution during numerical simulation. [**22**] Biasetti (2012) provides a model of the coagulation cascade as coupled reactions, supplies reaction rates for each, and simulates the production of thrombin in an abdominal aortic aneurysm (AAA) with the finite element method. [**4**]

The most comprehensive thrombosis models are those categorized as multiscale models. These models can combine different scales and modeling algorithms, such as using both Lagrangian and Eulerian methods. Fogelson (2008) proposed a two-scale thrombosis model for a stenosed vessel. The microscopic scale model tracked the motion and interaction of individual platelets with the fluid, vessel walls, and other platelets. Activation was simplified in that platelets in proximity to the injured wall immediately became activated, and adhesion was represented by an elastic link formed between the wall and the platelet. The macroscale model looks at the same interactions in terms of concentrations of platelets and distributions of adhesive and cohesive links. Both models used the immersed boundary method to simulate the platelet masses in the flow as it provided a way to include the influence of aggregate growth on the flow and calculate shear stresses more readily. [**11**] Xu (2008) developed a separate multiphase model in which the macroscale level employed the Navier-Stokes equations for the flow and advection-diffusion equations for chemicals, while the microscale model handled individual platelet activation, adhesion, and aggregation. The platelet interactions were solved using a cellular Potts model (CPM) at the microscale, which uses adhesion energy to simulate wall adhesion and platelet cohesion effects. [**43**] [**44**]

## 1.4 Stents

### 1.4.1 Overview

Coronary artery disease is considered the leading cause of mortality in the world. It involves the development of atherosclerotic lesions lining the artery wall, which as mentioned before, can go unstable and cause arterial thrombosis. Coronary arteries at risk are typically treated with percutaneous coronary intervention (PCI), which includes both balloon angioplasty of the vessel and stent implantation. [**17**]

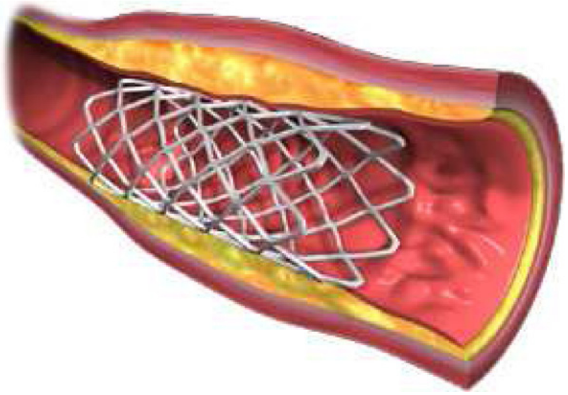

**Figure 4:** A stent placed inside an artery exhibiting stenosis. [**31**]

A stent is a tubular wire mesh structure that is designed to prop open a stenosed vessel over a long period of time. Initially, the treatment for coronary artery occlusion was to use only balloon angioplasty, a technique that inflates a balloon at the site of the stenosis and expands the artery locally to increase blood flow. However, balloon angioplasty by itself was not so effective because there was a very high risk for acute vessel closure immediately after the procedure due to elastic recoil, which could lead to acute myocardial infarction and other severe consequences just minutes after removal of the balloon. In addition, the balloon caused endothelial damage at the site of the angioplasty, which led to thrombosis. The first stent was implanted in a human body in 1986, and the first coronary stents were used in 1991 to treat acute myocardial infarction. They were initially designed to scaffold the dilated artery and prevent it from closing after balloon angioplasty. Today the vast majority of PCI procedures still use balloon angioplasty and stent implantation. [**17**]

It was discovered later that in-stent restenosis occurred in about 30% of coronary arteries with bare metal stents. This restenosis was due to two different phenomena. After angioplasty the damaged endothelium does induce a thrombotic response; however, this response is very effectively combated through antiplatelet and anticoagulant therapy delivered orally. But the response to injury, combined with the presence of a foreign body (the stent), triggers the formation and growth of neointima, a type of scar tissue that forms as inflammatory cells and then vascular smooth muscle cells are recruited to the site of the injury. [**41**] This complication was not as easily solved as early thrombosis effects. However, the development and implementation of drug-eluting stents (patented in 1997) proved to be a very effective tool in preventing restenosis from neointimal formation. [**9**] The drug-eluting stent is coated with drug-delivery vehicles to release chemicals slowly over time. The drug used to treat neointimal formation in clinical drug-eluting stents is sirolimus (formerly rapamycin), which is a potent inhibitor of vascular smooth muscle cell proliferation that causes arterial stenosis. Local delivery of the drug with appropriate release kinetics has significantly reduced the chance of restenosis of the artery; a 2002 study showed reduction of in-stent restenosis from 35.4% to 3.2%. [**41**]

### 1.4.2 Stent Thrombosis

Stent thrombosis was a serious complication in early PCI procedures, but antiplatelet and anticoagulant therapies have significantly reduced the major risks associated with balloon angioplasty and stent implantation. Nevertheless, stent thrombosis is still a medical problem, especially over longer periods of time.

Early stent thrombosis (EST) is defined as that which can be observed within the first 30 days after stent implantation. This was the complication that caused such high rates of restenosis and mortality in stent implantation in the 1980s and 1990s. The most effective tool in combating EST was found to be dual antiplatelet therapy with aspirin and the antithrombotic drug ticlopidine, which reduced the risk of early stent thrombosis to less than 2%. With the advent of drug-eluting stents, safety data showed similar or even lower rates of thrombosis with drug-eluting stents as compared to bare metal stents. However, a patient study showed a 1.4% rate of definite or probable stent thrombosis for both types of stents, indicating that although the risk of EST is low, it is nonzero. These risks are increased by procedural errors in the PCI procedure, pre- and post-treatments, and improper drug therapy delivery to the target. [**6**]

A complication that was discovered in the last two decades is that of late stent thrombosis (LST), defined as thrombosis occurring between one month and one year from stent implantation. While most of the risk factors for early stent thrombosis are procedural, those for LST are more often patient-specific, such as adverse cardiac events, increased rates of platelet aggregation, and impaired response to antiplatelet therapy. Obviously, discontinuation of the antiplatelet therapy is one of the biggest risk factors for LST. However, late and very late stent thrombosis (longer than one year after stent implantation) actually occur more commonly in drug-eluting stents than in bare metal stents. The reason for this appears to be delayed healing of the endothelium due to the drug-polymer combination released from the stent, which becomes a large risk factor if antiplatelet therapy is discontinued. If these complications are discovered, immediate action through another PCI procedure is the best therapy of choice to treat the thrombosis. [**40**]

### 1.4.3 Numerical Studies

Various models have been developed to investigate different aspects of stent implantation, local hemodynamics, and drug delivery from stents. One area of stent modeling research is to model the mechanical forces and interactions between the stent and the blood vessel. Kiousis (2007) developed a numerical model for the fissuring and dissection of the atherosclerotic plaque lining a human iliac artery in response to balloon angioplasty and stent placement. A three-dimensional finite element model was employed to model the angioplasty and stent contact forces, induced stresses on the arterial wall, and the gain in lumen area. [**20**] Zahedmanesh (2010) uses a three-dimensional finite element model to calculate the deformation and stresses present in the interaction between an expanding balloon and stent system and an arterial wall. [**45**]

Other models concern themselves primarily with the flow field over stented arteries. Berry (2000), one of the earlier numerical models of stents, is split into an experimental and a numerical section. The experiment uses dye visualization to investigate flow and shear rates in a synthetic coronary artery with an inserted stent. The numerical section uses computational fluid dynamics to model a two-dimensional pulsatile flow over the wires of a stent, and determines velocity and shear rate gradients in the channel for various different stent geometries. [**3**]

A third category of models specifically examines drug-eluting stents and analyzes how the drug is transported in the artery to its target tissue. Sakharov (2002) develops a mathematical model and simple numerical model for a stent-delivered drug that binds to vascular tissue. Diffusion properties of the drug and the mechanisms of binding are varied to study their effect on the biodistribution and pharmokinetics of the drug. [**34**] Zunino (2009) details a comprehensive model of drug distribution from a stent that includes mechanical action of the stent on the vascular wall and interaction of blood flow on drug release. The three-dimensional finite difference model is able to analyze the diffusion of the drug into the vascular tissue and how it is affected by these different factors. [**46**] Pontrelli (2010) investigates drug delivery effectiveness into the vascular tissue, treating the wall as four layers (endothelium, intima, elastic lamina, and media) that are porous to the drug and have their own diffusive properties. Through this model, analytical solutions for drug concentration and mass are obtained in space and time. [**31**] Vairo (2010) develops another comprehensive, multiscale and multidomain model for a drug-eluting stent that takes into account tissue microstructure and local hemodynamics to describe drug transport in stent coating, arterial tissue, and blood flow. The axisymmetric COMSOL model solves for flow velocity fields and drug concentrations given release dynamics, input blood flow, and wall porosity conditions. [**38**]

## 1.5 Objectives

There are two major objectives of the current study. First, this work will develop a numerical model for stent thrombosis based on computational fluid dynamics (CFD). The model will include an incompressible flow solver utilizing a sharp interface immersed boundary method to solve for the flow in a two-dimensional artery with stent geometry. This will be coupled to a scalar transport solver to solve the coupled advection-diffusion equations that describe the coagulation cascade and platelet adhesion/aggregation. Second, this numerical model will be applied to investigate the effectiveness of an anticoagulant based on its method of delivery. Antithrombin-bound heparin, an inhibitor of the coagulation cascade, will be administered both through the flow and through drug-eluting stents to the affected thrombogenic tissue. The model will be applied to both steady and pulsatile flow to compare the two delivery methods and quantitatively evaluate their effectiveness and efficiency in preventing the local platelet aggregation leading to stent thrombosis.

# 2 Methods

In this study, we use a computational model that couples an incompressible flow solver with a convection-diffusion-reaction equation model of the coagulation cascade and the Eulerian model of platelet activation and aggregation. We will investigate how platelet activation and aggregation are affected by the delivery of an anticoagulant both through the blood flow and through a drug-eluting stent for a two-dimensional stented artery.

## 2.1 Thrombosis Model

The model for thrombosis will incorporate the work of Biasetti (2012) and Leiderman (2011). Biasetti's model of the coagulation cascade will be used to determine thrombin concentration in the stented artery from a specified distribution of tissue factor representing the endothelium injured from balloon angioplasty. This thrombin concentration will then be used as an input to Leiderman's model of platelet deposition, where it will be used to activate mobile platelets in the blood. Leiderman's model will then describe the interplay between different species of platelets, the blood flow, and the affected endothelial wall in order to generate platelet adhesion and aggregation in response to vascular tissue injury.

### 2.1.1 Coagulation Cascade

Biasetti (2012) developed a fluid-chemical model to simulate the extrinsic pathway of the coagulation cascade through a series of coupled convection-diffusion-reaction equations. The model encompasses the various plasma-phase and surface-bound chemical species and reactions in the coagulation cascade. It was proposed initially to model thrombus formation in an abdominal aortic aneurysm, and was coupled with a shear-thinning incompressible flow model and solver for blood. In the current study, we employ the chemical modeling approach of Biasetti but use a Newtonian fluid model.

The coagulation cascade model begins after the binding of factor VIIa from the blood plasma with tissue factor (TF) on the subendothelium surface to form TF:VIIa. This begins a set of 16 distinct chemical reactions involving 18 different chemical species. The coupled convection-diffusion-reaction equations for the chemical species are written as:

$$\frac{\partial c_i}{\partial t} + \nabla \cdot \left(-D_i \nabla c_i\right) = R_i - \boldsymbol{u} \cdot \nabla c_i \qquad (1)$$

where $c_i$ for $i = 1, 2, \ldots, 18$ represents the species concentration, $D_i$ is the species diffusivity, and $\boldsymbol{u}$ is the flow velocity vector given from the Navier-Stokes equations (more information on this will be given in section 2.2.1). The concentration vector contains the 18 species in the following order: IX (antihemophilic factor B), TF:VIIa (tissue factor complex), IX:TF:VIIa ,IXa, X (Stuart-Prower factor), X:TF:VIIa, Xa, VIIIa:IXa, X:VIIIa:IXa, V (proaccelerin), Va, VIII (antihemophilic factor), VIIIa, IIa (thrombin), II (prothrombin), Va:Xa, II:Va:Xa, and mIIa. The reaction terms $R_i$ are defined by the individual 16 rate equations (equations (2)-(13)) and stoichiometric matrix $\mathbf{S}$. These specified reactions are all modeled to occur in the blood flow, not on any specific membranes or surfaces. Overall, the transport equation contains diffusion, reaction, and convection for each of the 18 chemical species. Table 1 contains the 18 reaction rates for the chemical equations.

$$\mathrm{IX + TF : VIIa} \underset{k_{16}}{\overset{k_6}{\rightleftarrows}} \mathrm{IX : TF : VIIa} \xrightarrow{\mathrm{k_{11}}} \mathrm{TF : VIIa + IXa} \tag{2}$$

$$\mathrm{X + TF : VIIa} \underset{k_{17}}{\overset{k_6}{\rightleftarrows}} \mathrm{X : TF : VIIa} \xrightarrow{\mathrm{k_{12}}} \mathrm{TF : VIIa + Xa} \tag{3}$$

$$\mathrm{X + VIIIa : IXa} \underset{k_{18}}{\overset{k_6}{\rightleftarrows}} \mathrm{X : VIIIa : IXa} \xrightarrow{\mathrm{k_{13}}} \mathrm{VIIIa : IXa + Xa} \tag{4}$$

$$\mathrm{IX + Xa} \xrightarrow{\mathrm{k_{15}}} \mathrm{Xa + IXa} \tag{5}$$

$$\mathrm{V + Xa} \xrightarrow{\mathrm{k_{1}}} \mathrm{Xa + Va} \tag{6}$$

$$\mathrm{VIII + Xa} \xrightarrow{\mathrm{k_{3}}} \mathrm{Xa + VIIIa} \tag{7}$$

$$\mathrm{V + IIa} \xrightarrow{\mathrm{k_{2}}} \mathrm{IIa + Va} \tag{8}$$

$$\mathrm{VIII + IIa} \xrightarrow{\mathrm{k_{4}}} \mathrm{IIa + VIIIa} \tag{9}$$

$$\mathrm{II + Va : Xa} \underset{k_{19}}{\overset{k_6}{\rightleftarrows}} \mathrm{II : Va : Xa} \xrightarrow{\mathrm{k_{14}}} \mathrm{Va : Xa + mIIa} \tag{10}$$

$$\mathrm{mIIa + Va : Xa} \xrightarrow{\mathrm{k_{5}}} \mathrm{Va : Xa + II} \tag{11}$$

$$\mathrm{VIIIa} + \mathrm{IXa} \underset{k_9}{\overset{k_7}{\rightleftarrows}} \mathrm{VIIIa}:\mathrm{IXa} \tag{12}$$

$$\mathrm{Va} + \mathrm{Xa} \underset{k_{10}}{\overset{k_8}{\rightleftarrows}} \mathrm{Va}:\mathrm{Xa} \tag{13}$$

| **Rate Constant** | **Value** |
|---|---|
| $k_1$ | $2 \times 10^4$ mol$^{-1}$ m$^3$ s$^{-1}$ |
| $k_2$ | $2 \times 10^4$ mol$^{-1}$ m$^3$ s$^{-1}$ |
| $k_3$ | $1 \times 10^4$ mol$^{-1}$ m$^3$ s$^{-1}$ |
| $k_4$ | $2 \times 10^4$ mol$^{-1}$ m$^3$ s$^{-1}$ |
| $k_5$ | $1 \times 10^4$ mol$^{-1}$ m$^3$ s$^{-1}$ |
| $k_6$ | $1 \times 10^5$ mol$^{-1}$ m$^3$ s$^{-1}$ |
| $k_7$ | $1 \times 10^4$ mol$^{-1}$ m$^3$ s$^{-1}$ |
| $k_8$ | $4 \times 10^5$ mol$^{-1}$ m$^3$ s$^{-1}$ |
| $k_9$ | 0.005 s$^{-1}$ |
| $k_{10}$ | 0.4 s$^{-1}$ |
| $k_{11}$ | 0.3 s$^{-1}$ |
| $k_{12}$ | 1.15 s$^{-1}$ |
| $k_{13}$ | 8.2 s$^{-1}$ |
| $k_{14}$ | 32 s$^{-1}$ |
| $k_{15}$ | $1 \times 10^2$ mol$^{-1}$ m$^3$ s$^{-1}$ |
| $k_{16}$ | 24 s$^{-1}$ |
| $k_{17}$ | 44 s$^{-1}$ |
| $k_{18}$ | 0.001 s$^{-1}$ |
| $k_{19}$ | 70 s$^{-1}$ |

**Table 1:** List of reaction rates for coagulation cascade model.

The governing equation for the actual coagulation cascade reaction model is $\frac{dc_i}{dt} = S_{ij} r_j$, where $\frac{d}{dt}$ represents the total derivative, $S_{ij}$ is the 18 × 16 stoichiometric matrix mentioned above and $r_j$ is the vector for the reaction rates in the 16 equations. The stoichiometric matrix coefficients determine the reactants and products of each equation as well as their ratio, and in this way reaction kinetics are incorporated into this time-evolving coagulation cascade model.

If the anticoagulant heparin is present, the model incorporates it in its active form bound with antithrombin to form AT:H. This adds a 19th species to the concentration, an extra diffusivity, and additional reaction vector terms in the convection-diffusion-reaction equations, and also changes the stoichiometric matrix to represent the inhibitory effect of the AT:H complex on various reactions in the coagulation cascade as shown below in Figure 5. The additional reactions are found in equations (14)-(16), and reaction rates for high-affinity heparin are found in table 2.

$$\mathrm{Xa} + \mathrm{AT:H} \xrightarrow{k_{20}} \mathrm{Xa:AT:H} \tag{14}$$

$$\mathrm{IXa} + \mathrm{AT:H} \xrightarrow{k_{21}} \mathrm{IXa:AT:H} \tag{15}$$

$$\mathrm{IIa} + \mathrm{AT:H} \xrightarrow{k_{22}} \mathrm{IIa:AT:H} \tag{16}$$

$$\begin{vmatrix}
-1 & 0 & 0 & 0 & 0 & 0 & -1 & 0 & 0 & 0 & 0 & 0 & 0 & 0 & 0 & 0 & 0 & 0 & 0 \\
-1 & 1 & -1 & 1 & 0 & 0 & 0 & 0 & 0 & 0 & 0 & 0 & 0 & 0 & 0 & 0 & 0 & 0 & 0 \\
1 & -1 & 0 & 0 & 0 & 0 & 0 & 0 & 0 & 0 & 0 & 0 & 0 & 0 & 0 & 0 & 0 & 0 & 0 \\
0 & 1 & 0 & 0 & 0 & 0 & 1 & 0 & 0 & 0 & 0 & 0 & 0 & 0 & -1 & 0 & -1 & 0 & 0 \\
0 & 0 & -1 & 0 & -1 & 0 & 0 & 0 & 0 & 0 & 0 & 0 & 0 & 0 & 0 & 0 & 0 & 0 & 0 \\
0 & 0 & 1 & -1 & 0 & 0 & 0 & 0 & 0 & 0 & 0 & 0 & 0 & 0 & 0 & 0 & 0 & 0 & 0 \\
0 & 0 & 0 & 1 & 0 & 1 & 0 & 0 & 0 & 0 & 0 & 0 & 0 & 0 & 0 & -1 & 0 & -1 & 0 \\
0 & 0 & 0 & 0 & -1 & 1 & 0 & 0 & 0 & 0 & 0 & 0 & 0 & 0 & 1 & 0 & 0 & 0 & 0 \\
0 & 0 & 0 & 0 & 1 & -1 & 0 & 0 & 0 & 0 & 0 & 0 & 0 & 0 & 0 & 0 & 0 & 0 & 0 \\
0 & 0 & 0 & 0 & 0 & 0 & 0 & -1 & 0 & -1 & 0 & 0 & 0 & 0 & 0 & 0 & 0 & 0 & 0 \\
0 & 0 & 0 & 0 & 0 & 0 & 0 & 1 & 0 & 1 & 0 & 0 & 0 & 0 & 0 & -1 & 0 & 0 & 0 \\
0 & 0 & 0 & 0 & 0 & 0 & 0 & 0 & -1 & 0 & -1 & 0 & 0 & 0 & 0 & 0 & 0 & 0 & 0 \\
0 & 0 & 0 & 0 & 0 & 0 & 0 & 0 & 1 & 0 & 1 & 0 & 0 & 0 & -1 & 0 & 0 & 0 & 0 \\
0 & 0 & 0 & 0 & 0 & 0 & 0 & 0 & 0 & 0 & 0 & 0 & 0 & 1 & 0 & 0 & 0 & 0 & -1 \\
0 & 0 & 0 & 0 & 0 & 0 & 0 & 0 & 0 & 0 & 0 & -1 & 0 & 0 & 0 & 0 & 0 & 0 & 0 \\
0 & 0 & 0 & 0 & 0 & 0 & 0 & 0 & 0 & 0 & 0 & -1 & 1 & 0 & 0 & 1 & 0 & 0 & 0 \\
0 & 0 & 0 & 0 & 0 & 0 & 0 & 0 & 0 & 0 & 0 & 1 & -1 & 0 & 0 & 0 & 0 & 0 & 0 \\
0 & 0 & 0 & 0 & 0 & 0 & 0 & 0 & 0 & 0 & 0 & 0 & 1 & -1 & 0 & 0 & 0 & 0 & 0 \\
0 & 0 & 0 & 0 & 0 & 0 & 0 & 0 & 0 & 0 & 0 & 0 & 0 & 0 & 0 & 0 & -1 & -1 & -1
\end{vmatrix}$$

**Figure 5:** The stoichiometric matrix $S_{ij}$ used for the reactions of the coagulation cascade and additional AT:H reactions.

| **Rate Constant** | **Value** |
|---|---|
| $k_{20}$ | $2 \times 10^4$ mol$^{-1}$ m$^3$ s$^{-1}$ |
| $k_{21}$ | $140 \times 10^3$ mol$^{-1}$ m$^3$ s$^{-1}$ |
| $k_{22}$ | $37 \times 10^3$ mol$^{-1}$ m$^3$ s$^{-1}$ |

**Table 2:** List of reaction rates for the high-affinity heparin reactions in the coagulation cascade model.

| **Species** | **Concentration** |
|---|---|
| IX | $90 \times 10^{-6}$ mol m$^{-3}$ |
| TF:VIIa | $1 \times 10^{-6}$ mol m$^{-3}$ |
| X | $170 \times 10^{-6}$ mol m$^{-3}$ |
| V | $20 \times 10^{-6}$ mol m$^{-3}$ |
| VIII | $0.7 \times 10^{-6}$ mol m$^{-3}$ |
| VIIIa | $0.1 \times 10^{-6}$ mol m$^{-3}$ |
| II | $1.4 \times 10^{-3}$ mol m$^{-3}$ |
| AT:H | $60 \times 10^{-6}$ mol m$^{-3}$ |

**Table 3:** Initial species concentrations of inputs for coagulation cascade model. All other species have zero initial concentrations.

Table 3 gives typical concentrations of the model inputs as provided by Biasetti, as well as a typical value for heparin concentration in the blood. Additionally, the diffusivity of the chemical species in the cascade according to Leiderman is $5 \times 10^{-7}\,\mathrm{cm}^2/\mathrm{s}$. The net result of this extrinsic coagulation cascade pathway model is the formation of IIa thrombin, which among other roles is used to activate platelets in the bloodstream.

### 2.1.2 Platelet Model

In Leiderman's work, a comprehensive platelet model is developed that considers the coagulation cascade, platelet activation, adhesion, aggregation, and even the blood flow interactions with the growing thrombus mass. Only the platelet model is used in this essay; the coagulation cascade model in Biasetti is substituted for blood coagulation and thrombin production, and the thrombus mass in our case is small and flat enough to minimally impact the blood flow. This model was tested for a two-dimensional parabolic blood inflow velocity profile, which is quite similar to the boundary conditions used in this stent model described in 2.3.2. Combining this model with the Biasetti coagulation cascade model will provide a full platelet deposition model that corresponds to thrombus formation.

Leiderman's model categorizes platelets in four distinct categories. Mobile, unactivated platelets $P^{m,u}$ are the free-flowing latent platelets naturally found in the bloodstream. Through activation by thrombin or ADP (not used in this essay's model), these are converted to mobile, activated platelets $P^{m,a}$. Platelets directly attached to the injured vascular wall through adhesion are subendothelium-bound activated platelets $P^{se,a}$, and platelets attached to other bound platelets are platelet-bound activated $P^{b,a}$. The transport equations for these four species are given by equations (17)-(20):

$$\begin{aligned}\frac{\partial P^{m,u}}{\partial t} &= -\nabla \cdot \left\{ W\left(\phi^{T}\right)\left(\boldsymbol{u}\, P^{m,u} - D \nabla P^{m,u}\right)\right\} - k_{adh}(\boldsymbol{x})\left\{P_{\max} - P^{se,a}\right\}P^{m,u} \\ &- A_1\left(c_{IIa}\right)P^{m,u}\end{aligned} \tag{17}$$

$$\begin{aligned}\frac{\partial P^{m,a}}{\partial t} &= -\nabla \cdot \left\{ W\left(\phi^{T}\right)\left(\boldsymbol{u}\, P^{m,a} - D \nabla P^{m,a}\right)\right\} - k_{adh}(\boldsymbol{x})\left\{P_{\max} - P^{se,a}\right\}P^{m,a} \\ &+ A_1\left(c_{IIa}\right)P^{m,u} - k_{coh}\, g(\eta) P_{\max} P^{m,a}\end{aligned} \tag{18}$$

$$\frac{\partial P^{b,a}}{\partial t} = -k_{adh}(\boldsymbol{x})\left\{P_{\max} - P^{se,a}\right\}P^{m,a} + k_{coh}\, g(\eta) P_{\max} P^{m,a} \tag{19}$$

$$\frac{\partial P^{se,a}}{\partial t} = -k_{adh}(\boldsymbol{x})\left\{P_{\max} - P^{se,a}\right\}\left(P^{m,u} + P^{m,a} + P^{b,a}\right) \tag{20}$$

where $\boldsymbol{u}$ is again the flow velocity vector, $D$ is the platelet diffusivity, $P_{\max}$ is a maximum number density for platelets (set to $6.67 \times 10^7$/mm$^3$), and $c_{IIa}$ is the concentration of IIa thrombin. The function $W\left(\phi^T\right) = \tanh\left(\pi\left(1-\phi^T\right)\right)$ is a function of platelet fraction that acts to slow down platelets moving through a platelet-rich region due to their size. The coefficients $k_{adh}$ and $k_{coh}$ are used in adhesion and cohesion of platelets, with the spatial dependence of the former being used to ensure that adhesion only occurs at the subendothelium. The activation rate function $A_1\left(c_{IIa}\right) = k_{c_{IIa}}^{pla} \frac{c_{IIa}}{c^* + c_{IIa}}$ is used, with $k_{c_{IIa}}^{pla}$ and $c^*$ being positive constants. The cohesion term also has a function $g(\eta)$ that represents a binding affinity function that governs the rate and distance at which platelets can bind to each other. In Leiderman's model this was done with the release of a virtual scalar $\eta$ that was secreted from subendothelium-bound and platelet-bound platelets, which would decay at some distance away from its source. This allowed bonds of a specified length to form between platelets. However, the model that was used for the stented artery used a numerical alternative to this virtual scalar approach, which is described in 0.

Rate constants and other parameters were fixed for this model as in section 2.3.3. Leiderman provides a diffusivity for platelets of $2.5 \times 10^{-7} \mathrm{cm}^2/\mathrm{s}$. Typical human platelet counts are in the range of $150 - 450 \times 10^{12}/\mathrm{m}^3$ for mobile unactivated platelets. Through this model bloodborne unactivated platelets will be activated by thrombin produced in the blood from the Biasetti model, and then those platelets will be able to bind to the subendothelium and create a growing clot model.

## 2.2 Numerical Methods

Numerical simulation of the coagulation cascade and platelet models above in a biological flow involves the fluid dynamics of a stented artery, the transport of biochemical species in such a flow, and the interaction of the species with each other. This problem requires a high-fidelity incompressible flow solver coupled with an advection-diffusion solver for the transport equations that describe the various biochemical reactions of thrombosis. In this section, details about the incompressible flow solver and the scalar transport solver are provided.

### 2.2.1 Incompressible Flow Solver

The flow solver in this study is the one described in Mittal (2008). [**26**] The fluid dynamics of blood flow are governed by the incompressible Navier-Stokes equations:

$$\frac{\partial u_i}{\partial x_i} = 0 \tag{21}$$

$$\frac{\partial u_i}{\partial t} + \frac{\partial \left(u_i u_j\right)}{\partial x_j} = -\frac{1}{\rho}\frac{\partial p}{\partial x_i} + \nu \frac{\partial}{\partial x_j}\left(\frac{\partial u_i}{\partial x_j}\right) \tag{22}$$

where $u_i$ are the velocity components for $i, j = 1, 2, 3$ (although we only consider a two-dimensional system, the solver is able to handle three-dimensional problems as well), $p$

is the pressure, $\rho$ is the fluid density, and $\nu$ is the kinematic viscosity. The boundary conditions for velocity are the no-slip condition on the walls of the channel, a zero-gradient outflow, and specified inflow conditions that will be described later. These equations are discretized appropriately in time and space to solve them on a Cartesian grid.

Equations (21)-(22) are discretized in space with a cell-centered, collocated finite difference scheme. Here, the values of velocity and pressure are stored at the centers of all cells. In addition, a set of face-center velocities $U_i$ are calculated at each time step by averaging the values at each grid node. The equations are discretized in time by using the fractional step method of Van-Kan, which is described below.

$$\frac{u_i^* - u_i^n}{\Delta t} + \frac{1}{2}\left(\frac{\delta\left(U_j^* u_i^*\right)}{\delta x_j} + \frac{\delta\left(U_j^n u_i^n\right)}{\delta x_j}\right) = -\frac{1}{\rho}\frac{\delta p^n}{\delta x_i} + \nu\frac{1}{2}\left(\frac{\delta}{\delta x_j}\frac{\delta u_i^*}{\delta x_j} + \frac{\delta}{\delta x_j}\frac{\delta u_i^n}{\delta x_j}\right) \tag{23}$$

$$\frac{1}{\rho}\frac{\delta}{\delta x_i}\left(\frac{\delta p'}{\delta x_i}\right) = \frac{1}{\Delta t}\frac{\delta U_i^*}{\delta x_i} \tag{24}$$

$$\frac{u_i^{n+1} - u_i^n}{\Delta t} = -\frac{1}{\rho}\frac{\delta p'}{\delta x_i} \tag{25}$$

$$p^{n+1} = p^n + p' \tag{26}$$

The Van-Kan fractional step method takes the velocity from $u_i^n$ to $u_i^{n+1}$ in a series of three substeps and an intermediate step $u_i^*$. In the first substep, the modified momentum equation (23) derived from (22) is solved. Here the advective and diffusive terms have been discretized with a Crank-Nicolson scheme, and $\frac{\delta}{\delta x}$ represents a second order difference operator. The face-center velocities are calculated by averaging the values at the grid nodes to either side of the face. Using face-center velocities eliminates the problem of odd-even decoupling that is associated with cell-centered, collocated grids.

In the second substep, a pressure correction term $p'$ is calculated from the newly-computed face-center velocities. This equation is obtained from combining the momentum equation (22) with the divergence-free velocity condition (21). As a result, proper numerical discretization ensures that the final velocity $u_i^{n+1}$ will be divergence-free. This Poisson equation for the pressure is solved for Neumann boundary conditions at all boundaries. The Poisson solver employs the multigrid method with a Gauss-Seidel line-SOR smoother, a method that is known to be highly efficient and quickly convergent. Its convergence scales almost linearly with the number of grid points.

After the pressure correction has been obtained, the final substep is to update the pressure and velocity from the intermediate step to the $n+1$ step. Equations (25) and (26) illustrate this procedure for velocity and pressure. The updated velocities satisfy mass conservation to machine accuracy and allow for quick simulation of a flow using a Cartesian grid.

## Immersed Boundary Method

To deal with the geometry of the curved stent wire structures, the solver employs a sharp interface immersed boundary method to apply the stent boundary conditions of no-slip and no-penetration onto the grid. Immersed boundary (IB) methods generally fall into two categories: continuous and discrete forcing approaches. Continuous forcing IB methods introduce a forcing term to account for the immersed boundary into the continuous governing equations, and then discretize the result for numerical solution. Discrete forcing methods, such as the one used here, first discretize the governing equations disregarding the immersed boundary, and then modify the discretization in cells close to the immersed boundary to account for its presence. In the current model, this is done with the use of ghost cells with values determined to match boundary conditions locally.

The stent geometry is represented by an unstructured mesh of triangular elements generated using the meshing software Gambit. First, the grid cells are separated into "solid cells" and "fluid cells:" those whose cell centers lie inside the solid boundary defined by the mesh, and those whose cell centers lie outside the body. This is done for a specific node by determining the surface element closest to the node and then taking the dot product of the surface normal $\hat{n}$ with the vector $\vec{p}$ extending from the surface element to the node. A positive value of $\vec{p} \cdot \hat{n}$ indicates that the node is outside the solid body, and a negative value shows that it lies within the body. After this, cells are identified as "ghost cells" from the solid cells if they have a neighboring fluid cell in any direction. Figure 6 shows the identification of solid, fluid, and ghost cells for a curved boundary.

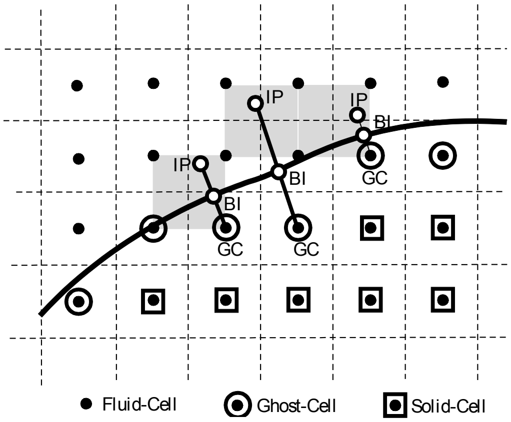

**Figure 6:** A depiction of the sharp interface immersed boundary method used in this simulation. The fluid, solid, and ghost cells (GC) are depicted, as well as the image points (IP) and boundary intercepts (BI) utilized by the solver. This figure has been taken from Mittal (2008). [**26**]

The procedure now is to obtain a value for each ghost cell that will ensure implicit satisfaction of the boundary conditions for the solid body. To do this, an appropriate boundary intercept is found for the ghost cell such that the intercept is both as close to the ghost cell node as possible and the intercept vector is as normal to the surface as possible. After obtaining the intercept, a "probe" is extended into the fluid domain to identify an image point such that boundary intercept is the midpoint of the segment connecting the ghost cell and image point. It is important that the image point be located close to the boundary such that it accurately reflects the local flow conditions of the boundary. Figure 6 shows the placement of boundary intercepts and image points for sample ghost points inside a curved boundary.

Next, we determine a value for the image point by using bilinear interpolation (trilinear in three dimensions) of the values of the nodes surrounding the image point. This is represented for each image point in Figure 6 as a gray box. This gives a value for the image point in the form $\phi_{IP} = \sum_i \beta_i \phi_i$, where $i$ represents the nodes used for interpolation and $\beta_i$ are the respective interpolation coefficients. After the value of the image point is obtained, it is straightforward to determine a ghost cell value that implicitly satisfies boundary conditions on the surface. For a Dirichlet condition, $\phi_{GC} = 2\phi_{BI} - \phi_{IP}$ determines the value of the ghost cell from the known value at the boundary intercept. For a Neumann condition, $\phi_{GC} = \phi_{IP} - \Delta l \left(\frac{\delta\phi}{\delta n}\right)_{BI}$, where $\Delta l$ is the probe length and $\left(\frac{\delta\phi}{\delta n}\right)_{BI}$ is the known flux at the boundary. These expressions are all second order accuracy, and can be used to solve the velocity and pressure equations at the stent wire boundaries in this simulation.

### 2.2.2 Scalar Transport Solver

The convection-diffusion-reaction equation (1) is coupled to the incompressible flow solution via the term $\boldsymbol{u}$. At each time step, the flow solution is then used in the calculation of the coupled equations for transport of each chemical species. Species are coupled by writing them into a nonlinear system of equations for a species concentration vector at each cell node. This equation is solved at the cell centers using a fully explicit fourth-order Runge-Kutta time discretization, with the convection term being spatially discretized by the following second-order upwind scheme for the first derivative. At each time step, the first order ODE in (28) is solved by first calculating the intermediate quantities in (29)-(32) and then advancing the concentration from time step $n$ to $n+1$ as in (33). Here $f(c,t)$ represents the right hand side of (28), which is spatially discretized and evaluated for each of the increments in the quantities $k_1$-$k_4$.

$$\left.\frac{\partial \phi}{\partial x_i}\right|_{x_i} \approx \frac{3\phi_i - 4\phi_{i-1} + \phi_{i-2}}{2\,\Delta x} \tag{27}$$

$$\frac{\partial c}{\partial t} = \nabla \cdot \left(D \nabla c\right) + R - \boldsymbol{u} \cdot \nabla c \equiv f(c,t) \tag{28}$$

$$k_1 = \Delta t\, f\left(c_n, t_n\right) \tag{29}$$

$$k_2 = \Delta t\, f\left(c_n + \frac{k_1}{2}, t_n + \frac{\Delta t}{2}\right) \tag{30}$$

$$k_3 = \Delta t\, f\left(c_n + \frac{k_2}{2}, t_n + \frac{\Delta t}{2}\right) \tag{31}$$

$$k_4 = \Delta t\, f\left(c_n + k_3, t_n + \Delta t\right) \tag{32}$$

$$c_{n+1} = c_n + \frac{1}{6}\left(k_1 + 2k_2 + 2k_3 + k_4\right) \tag{33}$$

## 2.3 Simulation Parameters

The model described above is applied to the specific problem of a stented artery through the development of a channel and stent geometry, flow boundary conditions, and chemical species boundary conditions. The study examines both steady and pulsatile flow through a two-dimensional channel representing a coronary artery containing a series of stent wires. For both types of flow the model will simulate three cases:

a. A bare metal stent control case with no anticoagulant.

b. A bare metal stent with antithrombin-heparin complex anticoagulant delivered through the flow.

c. A drug-eluting stent secreting the same antithrombin-heparin complex into the flow.

### 2.3.1 Channel and Stent Geometry

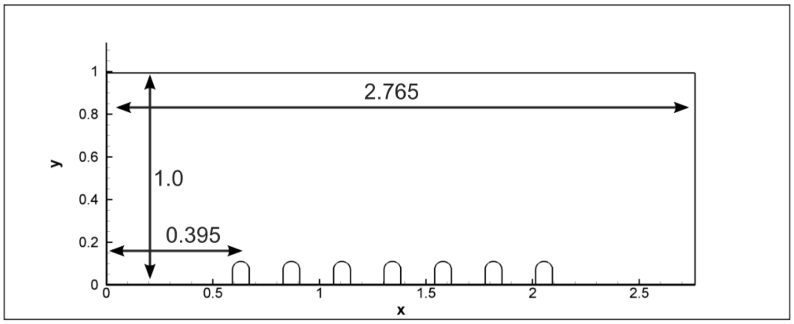

**Figure 7:** A diagram of the 2D half-channel with stent geometry used in numerical simulation. The lengths are normalized in accordance with Berry (2000) such that the height of the half-channel (1.0) is 1 mm.

The numerical study describes the coronary artery as a two-dimensional channel, and uses the work of Berry (2000) as a foundation. [**3**] A number of simplifications are made in order to reduce the computational cost of the simulations. First, the tubular lumen is simplified to a 2D channel. Second, the flow in the channel is assumed to be symmetric about the centerline and only the bottom half of the channel is simulated. Figure 7 shows a diagram of the full channel simulated. The left and right sides indicate inflow and outflow, and on the bottom there is a boundary extending from the wall to indicate the geometry of the struts of the stent. The strut wire cross-section is circular, but Berry's work looked at the overlapping region of two stent struts, with the bottom wire being embedded slightly into the vessel wall. Here, this structure is simplified to the one seen in Figure 8 for the purposes of computational simplicity. Simulations were carried out with a two-wire structure that more closely resembled Berry's stent geometry, but no major differences were noted in the flow properties between that structure and the one used in the current study.

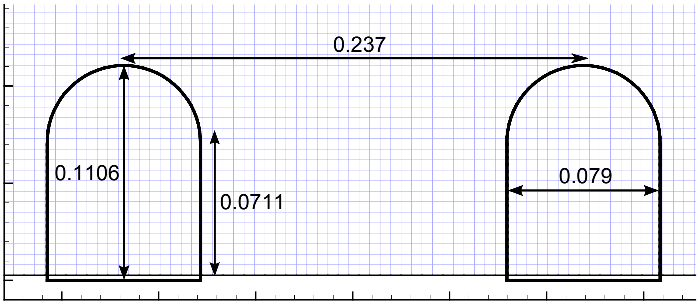

**Figure 8:** A diagram of the stent structure geometry with labeled dimensions overlaid on the computational grid. The lengths are normalized such that 1.0 represents 1 mm.

The length and height of the half-channel were taken to be 2.765 and 1.0 respectively. These lengths were obtained from Berry's work such that the height of the half-channel represents 1 mm. The width and spacing of the stent struts were taken from Berry's work as $w = 0.079$ and $3w = 0.237$, and the height of the structures was 0.1106. [**3**] The first stent structure is located at $5w = 0.395$ as shown in Figure 7. Figure 8 shows the relevant stent measurements. The simulation was performed on a 512 × 128 mesh with uniform spacing in the horizontal direction and geometrically-expanding intervals in the vertical direction past the height of the stent. This mesh was chosen such that the width of the stent structures would span about 15 grid horizontal grid lengths, which was assumed to be fine enough to capture all relevant features of the flow and transport model.

### 2.3.2 Flow Properties and Boundary Conditions

The simulations are performed for both a steady flow and a pulsatile flow. Obviously, blood flow in the coronary artery is inherently pulsatile, but here both cases will be studied to investigate the effect of pulsatile flow on any trends observed. The two dimensionless numbers of note are the Reynolds number and the Womersley number. The Reynolds number indicates the ratio of inertial to viscous forces in the flow, and is defined here by $\mathrm{Re} = \frac{U_c L}{\nu}$ where $U_c$ is the average fluid velocity at the inflow, $L$ is the channel height (here $L = 2.0$), and $\nu$ is the kinematic viscosity of the fluid. The Reynolds number used was $\mathrm{Re} = 160$ for a typical coronary artery under resting conditions for the heart, and is taken from Berry (2000). The Womersley number relates the pulsatile inertial forces to viscous forces in the flow. It is defined as $\mathrm{Wo} = \frac{L}{2}\sqrt{\frac{\omega}{\nu}}$ where $\omega$ is the angular frequency of the flow pulsation. For the current simulations, the value used is $\mathrm{Wo} = 2.7$ for resting conditions, in accordance with the work of Berry (2000). [**3**]

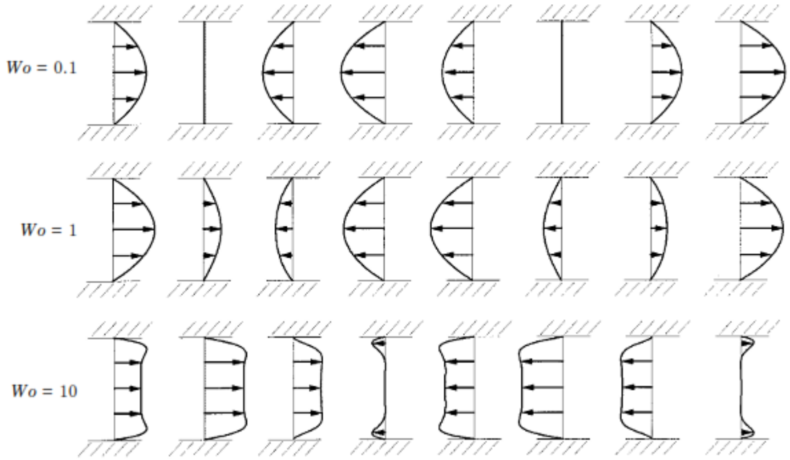

**Figure 9:** An illustration of sample flow profiles for Womersley numbers of 0.1, 1, and 10. This figure has been taken from Loudon (1998). [**25**]

A steady input flow was constructed using the fully developed Poiseuille flow solution for a channel. The pulsatile flow naturally occurring in the coronary artery is a reflection of varying pressure gradient, whose solution for pipe flow and a constant frequency change is known as the Womersley profile. However, in this study the pulsatile flow will be assumed as a sinusoidal form of the Poiseuille flow profile, since the Womersley number is not very high. Figure 9 shows why this is a reasonable assumption to make, as the Womersley number of 2.7 is closest to the $Wo = 1$ case where the flow is still parabolic. This treatment also provides easier implementation and faster simulation times. The amplitude of the pulsatile component is taken to be half that of the steady flow. Equations (27) and (28) are used for the steady and pulsatile input flows respectively, where $U_c$ is the mean velocity at the inflow used in the Reynolds number expression.

$$u_{steady}(y) = 1.5 U_c y(2.0 - y) \tag{34}$$

$$u_{puls}(y) = 1.5 U_c y(2.0 - y)(1.0 + 0.5\sin(2\pi\omega t)) \tag{35}$$

The velocity $U_c$ and frequency $\omega$ were determined from simulation parameters and the definitions of Reynolds and Womersley number. Table 4 gives the values of some of these simulation parameters for the flow.

| **Parameter** | **Values** |
|---|---|
| Kinematic viscosity $\nu$ | 0.0033 |
| Mean velocity $U_c$ | 0.2640 |
| Centerline velocity $u(y = 1.0)$ | 0.3960 |
| Characteristic time $l_{channel} / U_c$ | 10.4735 |
| Angular Frequency $\omega$ | 0.02451 |
| Period $1/\omega$ | 40.8047 |

**Table 4:** Dimensionless simulation parameters used for the flow in this study.

The boundary condition at the outflow was prescribed as a zero-flux condition, i.e. $\frac{\partial \boldsymbol{u}}{\partial x} = \frac{\partial \boldsymbol{u}}{\partial y} = 0$. At the top boundary, the "centerline" of the channel flow, a symmetry condition is applied such that $\frac{\partial u_x}{\partial y} = 0$ and $u_y = 0$.

### 2.3.3 Thrombosis Model Boundary Conditions

For the thrombosis model, the inputs needed are tissue factor sources, heparin sources, and the concentrations of inactivated platelets and various bloodborne intermediates in the coagulation cascade. The tissue factor is secreted from the injured tissue wall after balloon angioplasty. In the current simulation it is specified as a region along the bottom wall spanning from 0.4000 to 2.2910, an interval that encloses all of the stent structures. Using an immersed boundary object along the bottom wall with node spacing smaller than the grid spacing, the value for the tissue factor concentration of 100.0 is applied at each node (all simulation concentrations have been scaled such that unity in the simulation represents $1 \times 10^{-6}$ mol $m^{-3}$).

The study investigates two different methods of heparin delivery. For the case of flow-delivered heparin, the concentration of AT:H complex is specified initially everywhere in the fluid domain. Additionally, the same value is applied as a Dirichlet condition for AT:H concentration on the inflow boundary. For the case of heparin delivered by drug-eluting stents, the AT:H complex concentration value is specified as a Dirichlet condition on the boundaries of the stent struts. Just as with tissue factor, the value is specified at the nodes of the structure, and the node spacing is smaller than the grid spacing. In both cases the applied value of AT:H complex is 60.0.

The inactive platelet number density, as well as the concentrations of selected intermediates in the coagulation cascade that reside naturally in the blood, are also specified initially throughout the fluid domain. Just as with flow-delivered heparin, a Dirichlet condition is applied at the left inflow boundary with the same value as the initial concentration. The values of all of these species can be seen in table 5. All other species have zero initial concentration.

Platelet species and chemical species in this model have different diffusivities, and this is taken into account through the Schmidt number. The Schmidt number is the ratio of momentum diffusivity to mass diffusivity, and is defined here as $\mathrm{Sc} = \frac{\nu}{D}$. It is taken to be 400.0 for all chemical species and 4000.0 for all platelet species. The high Schmidt numbers should not cause stability concerns as the use of a second-order upwinding scheme will suppress numerical instabilities that may arise. A summary of all of these concentrations and Schmidt numbers is found in table 5.

| **Species** | **Initial Concentration/Number Density** | **Schmidt Number** |
|---|---|---|
| IX | 90.0 | 400.0 |
| TF:VIIa | 100.0 | 400.0 |
| X | 170.0 | 400.0 |
| V | 20.0 | 400.0 |
| VIII | 0.7 | 400.0 |
| VIIIa | 0.1 | 400.0 |
| II | 1400.0 | 400.0 |
| AT:H (in appropriate cases) | 60.0 | 400.0 |
| Mobile, unactivated platelets | 0.003748 | 4000.0 |
| All other platelet species | 0.0 | 4000.0 |
| All other chemical species | 0.0 | 400.0 |

**Table 5:** Summary of simulation initial conditions and boundary conditions for the thrombosis model. The coagulation cascade species concentrations are scaled such that unity represents $1 \times 10^{-6}$ mol $\mathrm{m}^{-3}$, and the platelet species number densities are normalized by the maximum allowed number density.

# 3 Results and Discussions

This section details the results of the thrombosis model simulation. First, the results of the flow simulation in the stented channel are presented for steady and pulsatile input flow profiles. Then, results from the modeling of the coagulation cascade and platelet adhesion and aggregation are shown for steady and pulsatile flow. For each flow type, three cases are investigated: a bare metal stent with no anticoagulant, a stent with flow-delivered AT:H complex, and a drug-eluting stent that delivers AT:H locally.

## 3.1 Flow Simulation Results

### 3.1.1 Steady Flow

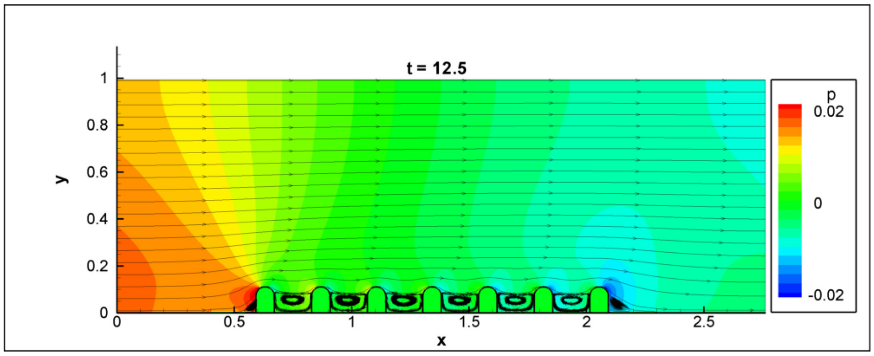

**Figure 10:** Pressure contours and streamlines for steady flow. After time $t = 12.5$ shown, the flow becomes steady in time.

The simulation results for steady parabolic input flow are shown above. Figure 10 shows the pressure contours and streamlines for the flow. The time $t = 12.5$ is used, after which the solution is steady. Comparing this to the characteristic time in Table 4 of 10.4735, there is good agreement as this is the first sampled time step after the characteristic time.

Inspecting the streamlines shows the characteristic recirculation zones between stent structures that were observed in Berry (2000). [**3**] Between each pair of structures is a clockwise-rotating vortex. These streamlines show that although the stent geometry was simplified from the one in Berry's paper, the major flow structures are still captured in this simulation.

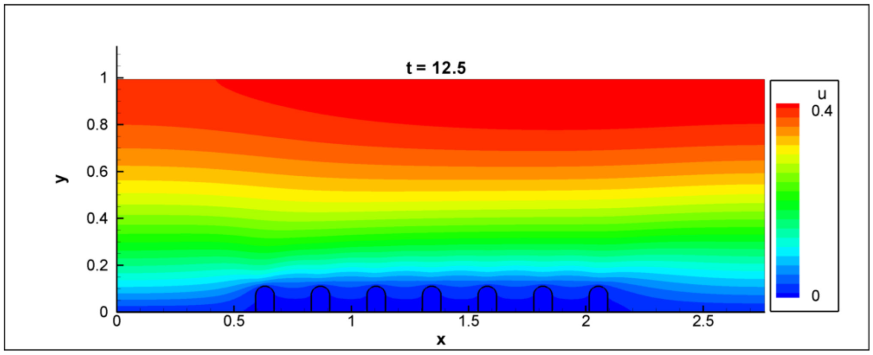

**Figure 11:** Horizontal velocity contours for steady flow. The flow is steady after time $t = 12.5$ shown.

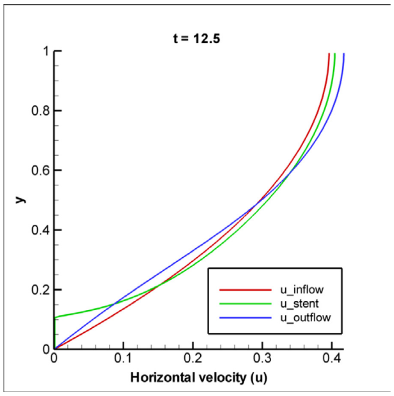

**Figure 12:** Plot of horizontal velocity profiles at three locations for steady flow. The inflow horizontal velocity is the simulation velocity at the cell centers immediately adjacent to the inflow, while the outflow horizontal velocity is the simulation velocity at the cell centers adjacent to the outflow. The stent horizontal velocity is the velocity through the line that cuts through the head of the first stent wire.

Figure 11 shows horizontal velocity contours for the entire domain, which indicates a roughly parabolic profile throughout the domain as expected. Figure 12 contains horizontal velocity profile plots at three locations: the inflow, outflow, and location of the first stent. Inspection shows that the no-slip boundary condition is obeyed at all three locations, and also shows a slight change in profile as the flow traverses the computational domain. Specifically, flow is channeled from the near-wall region towards the center of the channel as a result of interaction with the stent geometry.

### 3.1.2 Pulsatile Flow

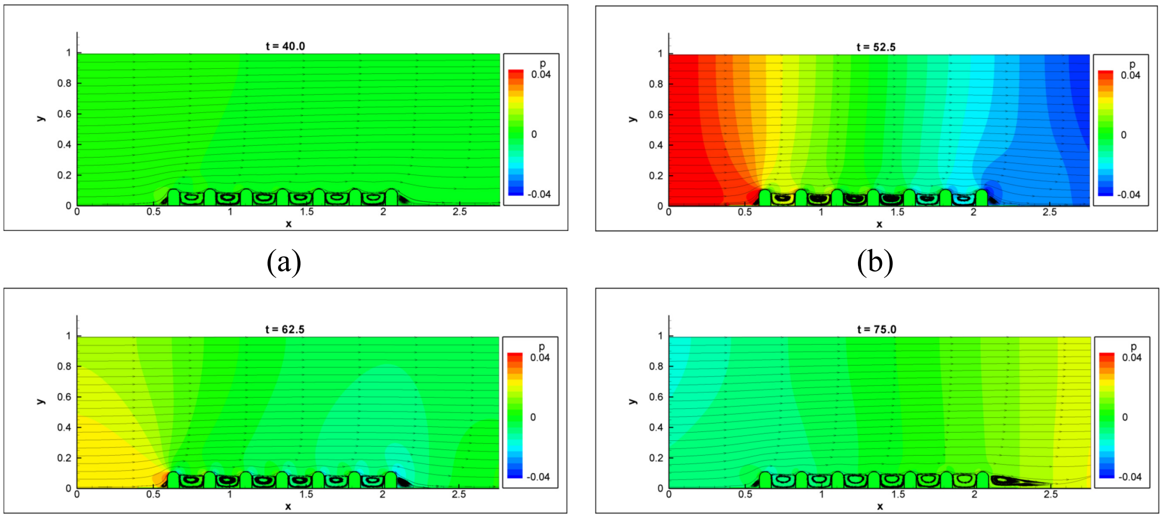

(a) (b)

(c) (d)

**Figure 13:** Pressure contours and streamlines for pulsatile flow. Four times are shown over the course of the simulation period: (a) $t = 40.0$, (b) $t = 52.5$, (c) $t = 62.5$, and (d) $t = 75.0$.

The simulation results for pulsatile flow are now shown. To illustrate the time dependence throughout the cycle period 40.8047, four time instants at 40.0, 52.5, 62.5, and 75.0 are chosen. Figure 13 shows the pressure contours and streamlines for pulsatile flow. The periodic pressure changes over time can be observed. At its peak in figure 13 (b), the pressure drop is roughly twice the magnitude of the drop for the steady case, and at its low point in figure 13 (a) it is almost zero. Throughout the course of the simulation the recirculation zones can be observed as in the steady case. However, at the end of the simulation period as shown in figure 13 (d), the streamlines to the right of the last stent strut lift upwards. This is connected with the reduction in horizontal velocity magnitude discussed below.

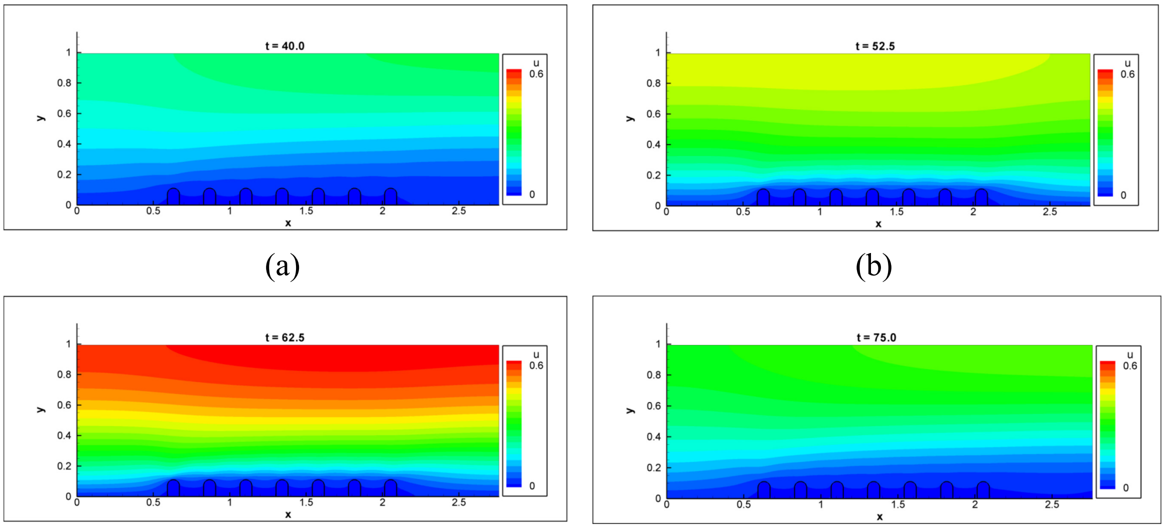

(a) (b)

(c) (d)

**Figure 14:** Horizontal velocity contours for pulsatile flow. Four times are shown over the course of the simulation period: (a) $t = 40.0$, (b) $t = 52.5$, (c) $t = 62.5$, and (d) $t = 75.0$.

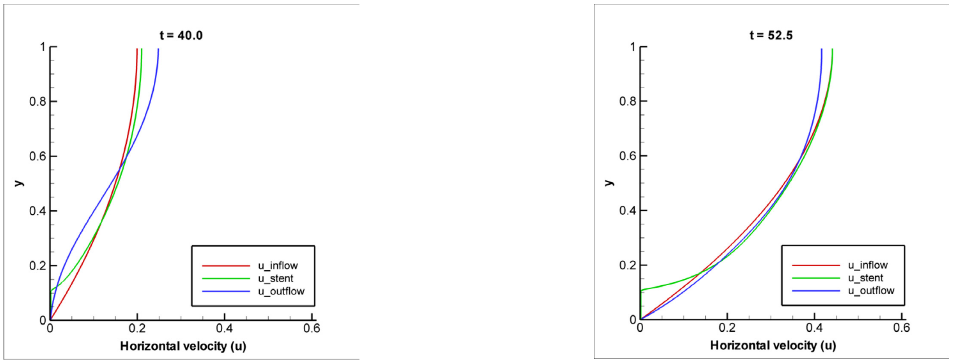

(a) (b)

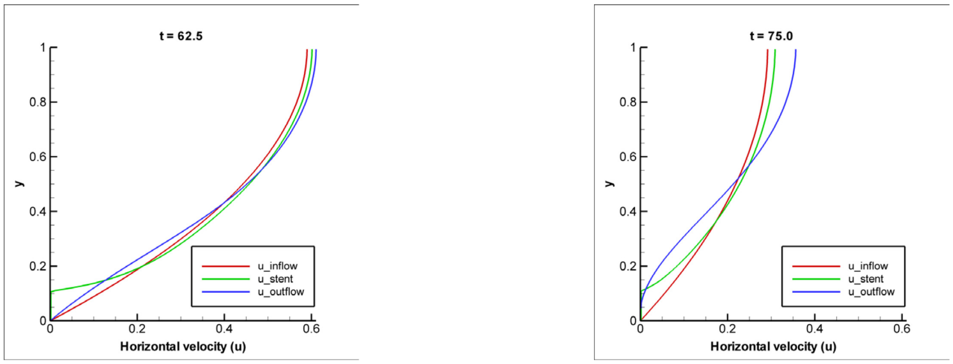

(c) (d)

**Figure 15:** Plot of horizontal velocity profiles at three locations for pulsatile flow. The inflow horizontal velocity is the simulation velocity at the cell centers immediately adjacent to the inflow, while the outflow horizontal velocity is the simulation velocity at the cell centers adjacent to the outflow. The stent horizontal velocity is the velocity through the line that cuts through the head of the first stent wire. Four times are shown over the course of the simulation period: (a) $t = 40.0$, (b) $t = 52.5$, (c) $t = 62.5$, and (d) $t = 75.0$.

Figure 14 shows the horizontal velocity contours over the simulation period. Upon comparison to the pressure contours, it can be observed that the peak magnitudes for velocity lag behind those for pressure. This behavior indicates that the simulation method used is effective for simulating a pressure-driven flow even though the time-varying pressure drop was not used for the boundary condition at the inflow and outflow. Figure 15 shows the horizontal velocity profiles over time again at three locations: the inflow, outflow, and location of the first stent. From figure 15 (c) we observe that the peak horizontal velocity is about 1.5 times that of the steady case, and from figure 15 (a) that the lowest horizontal velocity is roughly 0.5 times that of the steady case. This is exactly what is expected from our specified input flow. Also, we observe that at the outflow, the curvature of the flow closer to the wall is changing over time. These changes resemble the Womersley profile that is typical for flows created from pulsatile pressure drops. However, the flow over the first stent strut in figure 15 follows more of a parabolic shape, whose curvature indicates that the stent struts are not interacting with a developed Womersley flow. This is a difference between this simulation and biological blood flows, but its effect is assumed to be minor on the results obtained.

## 3.2 Thrombosis Modeling Results

The results from modeling the coagulation cascade and platelet clotting are presented in this section. The coagulation cascade is triggered by the release of tissue factor from the area of the wall specified as injured from the angioplasty procedure. Platelet species are tracked throughout the model, including mobile, activated platelets and platelets bound to the wall or to other platelets. The simulation is run for bare metal stents with no added heparin complex, AT:H delivered through the flow, and stent-delivered AT:H in order to determine the effectiveness of both anticoagulant delivery methods in reducing platelet activity. The simulation is run up to time $t = 500.0$.

### 3.2.1 Steady Flow

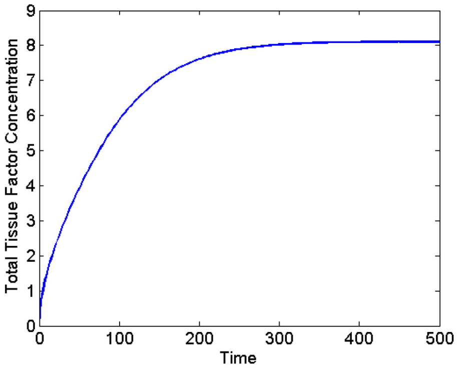

**Figure 16:** Plot of total tissue factor concentration in the domain over time for steady flow.

Figure 16 plots the total tissue factor concentration in the computational domain over time. It monotonically increases and plateaus over time as expected for the fixed-value of tissue factor at the boundary. All of the analysis is performed after the scalar concentrations have reached a steady state.

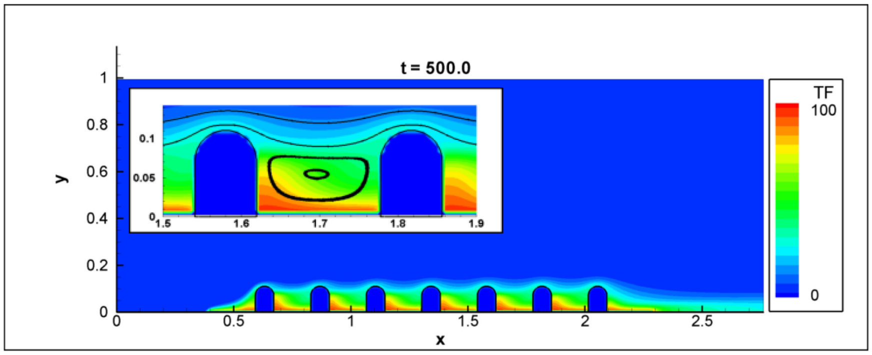

**Figure 17:** Tissue factor contours at time $t = 500.0$ for steady flow. The inset is zoomed on the region between struts 5 and 6, and includes streamlines for comparison.

Figure 17 shows contours of tissue factor at time 500.0 for steady parabolic inflow. The figure indicates that tissue factor has diffused into the flow from the lower wall between $x = 0.400$ and $x = 2.291$, where advection from interaction with the flow (diffusion is a lesser effect based on the high Schmidt numbers) leads to the distribution observed. Tissue factor is advected downstream, but the areas of high concentration remain close to the stent bodies. In between the struts, the highest concentration of tissue factor is found near the bottom of the leading strut, as the tissue factor near the trailing strut is more easily convected downstream.

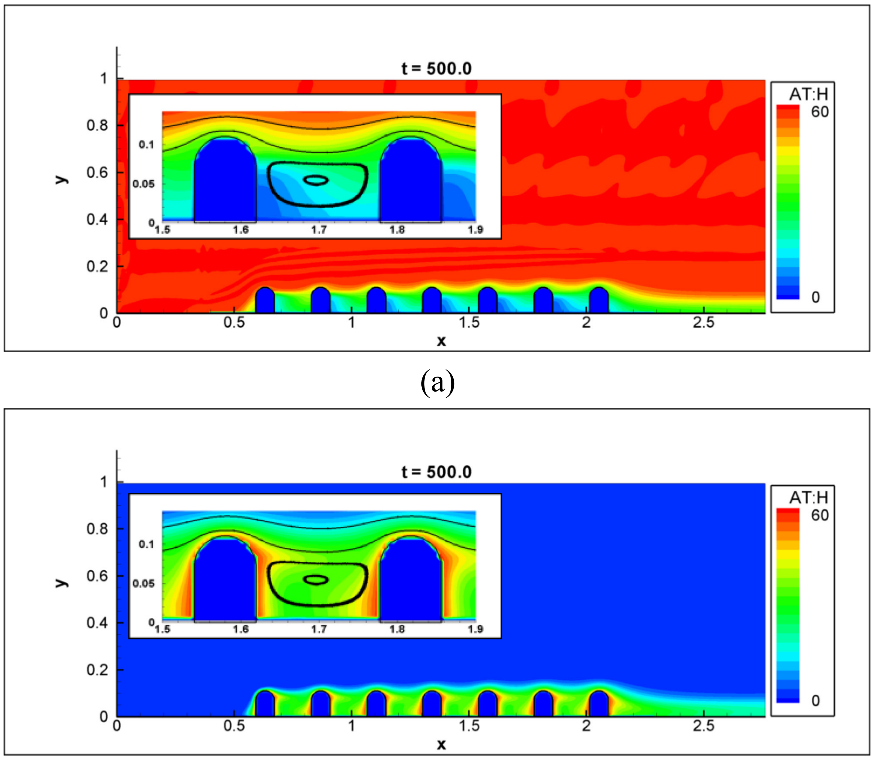

(a)

(b)

**Figure 18:** AT:H contours for (a) flow-delivered AT:H, and (b) drug-eluting stent-delivered AT:H at time $t = 500.0$ for steady flow. The insets are zoomed on the region between struts 5 and 6, and include streamlines for comparison.

Figure 18 shows the antithrombin-heparin complex contours at time 500.0 for two cases: in (a), the AT:H is delivered by the flow through a Dirichlet condition on the left boundary and in (b), the AT:H is delivered by a drug-eluting stent, modeled through a boundary condition on the stent struts. In both cases the anticoagulant diffuses into the flow, where it is transported primarily through advection through the domain. Figure 18 (a) shows that although there is a high concentration of heparin in the domain, it does not penetrate well into the region between the struts. Additionally, a very low concentration of AT:H is observed near the bottoms of the trailing edges of several stent struts (which also corresponds to the areas of maximum thrombin concentration as shown below) as the anticoagulant is advected into each recirculation zone from the left. The AT:H in the bulk flow is not effective in penetrating the vortices between stents to enter these regions, and whatever does enter is used up immediately in reactions with coagulation cascade intermediates. However, in figure 18 (b) there are higher AT:H concentrations in these regions with the drug-eluting stent, which means that it is not being used up entirely and that AT:H from the stents is more effectively moved by the flow to replace the anticoagulant used up in reactions.

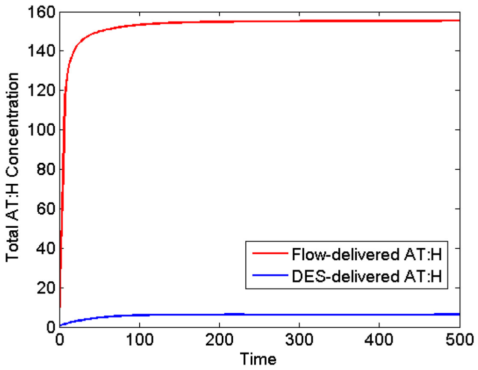

**Figure 19:** Plot of total AT:H concentration in the domain over time for steady flow.

Figure 19 shows the total AT:H concentration in the domain for both delivery methods. In both cases, the concentration increases and then plateaus, with values of roughly 155 and 6 for the flow-delivered and drug-eluting stent-delivered anticoagulant cases respectively. The drug-eluting stent releases significantly less anticoagulant into the channel than flow delivery, but a greater concentration is nonetheless delivered to the regions close to the stent structures.

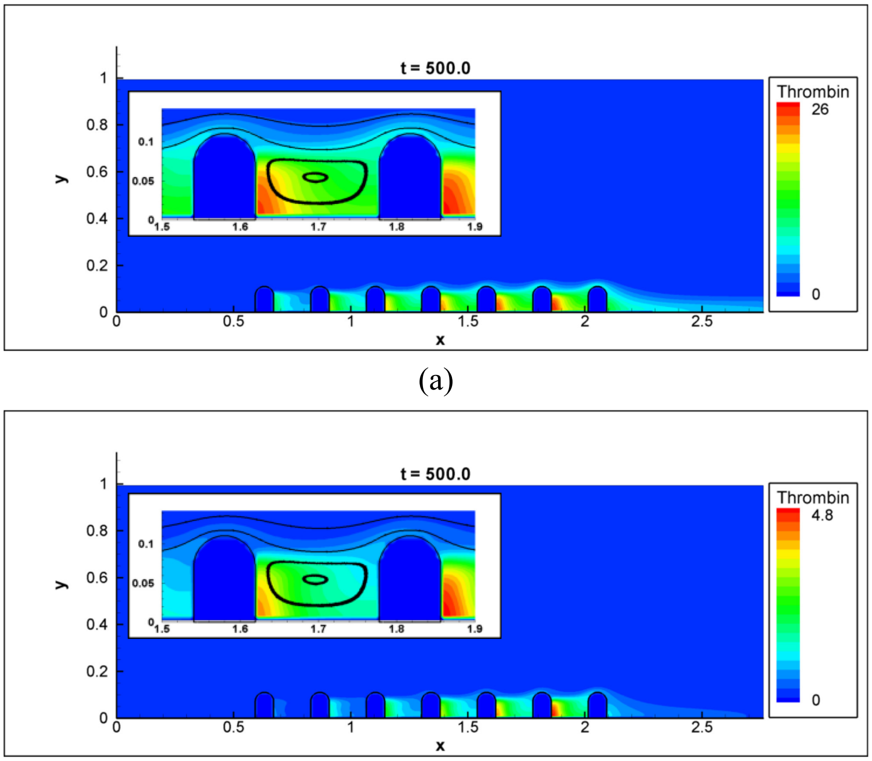

(a)

(b)

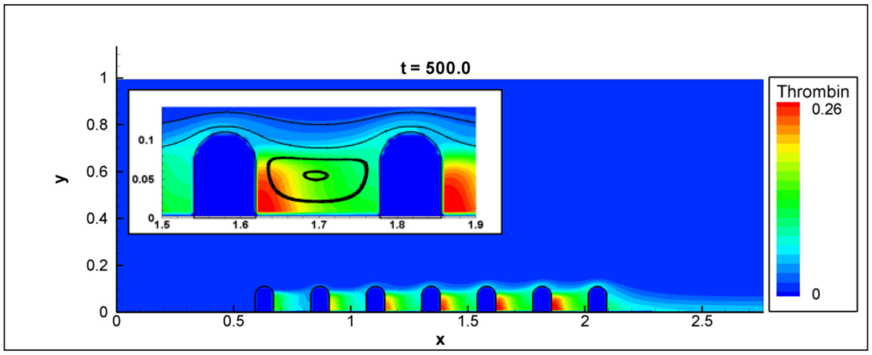

(c)

**Figure 20:** Thrombin contours for (a) bare metal stent, (b) flow-delivered AT:H, and (c) DES-delivered AT:H at time $t = 500.0$ for steady flow. The insets are zoomed on the region between struts 5 and 6, and include streamlines for comparison.

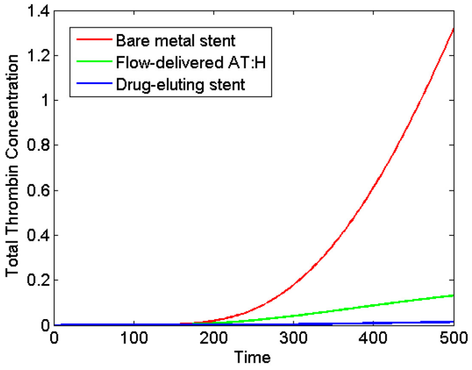

**Figure 21:** Plot of total thrombin concentration over time in the domain for bare metal stent, flow-delivered AT:H, and DES-delivered AT:H for steady flow.

Figure 20, depicts the contours of thrombin, mobile activated platelets, and bound platelets respectively throughout the domain at time 500.0 for the three cases. The production of thrombin takes into account reactions with the anticoagulant, so it is expected that the areas of higher thrombin concentration correlate with the regions of low heparin concentration, which is what is observed. The shapes of the contours are very similar for the three cases of bare metal stent, flow-delivered AT:H, and DES-delivered AT:H. The flow-delivered heparin case varies very slightly from the other two cases in that the thrombin concentration between the stent structures decreases more sharply from the base of the first strut's trailing edge to the top of the second strut. In all cases the concentrations are higher further downstream, which is because some of the thrombin and coagulation cascade intermediates from upstream are carried downstream by the flow. However, the concentration magnitudes are largely different. The peak concentrations of thrombin are roughly 26, 4.8, and 0.26 from the contour figures.

Figure 21 is a plot of total thrombin concentration in the domain, and shows the difference in concentration between the three cases. Both the flow-delivered AT:H and DES-delivered AT:H cases demonstrate significant reduction in thrombin production, but the drug-eluting stent delivery is clearly more effective.

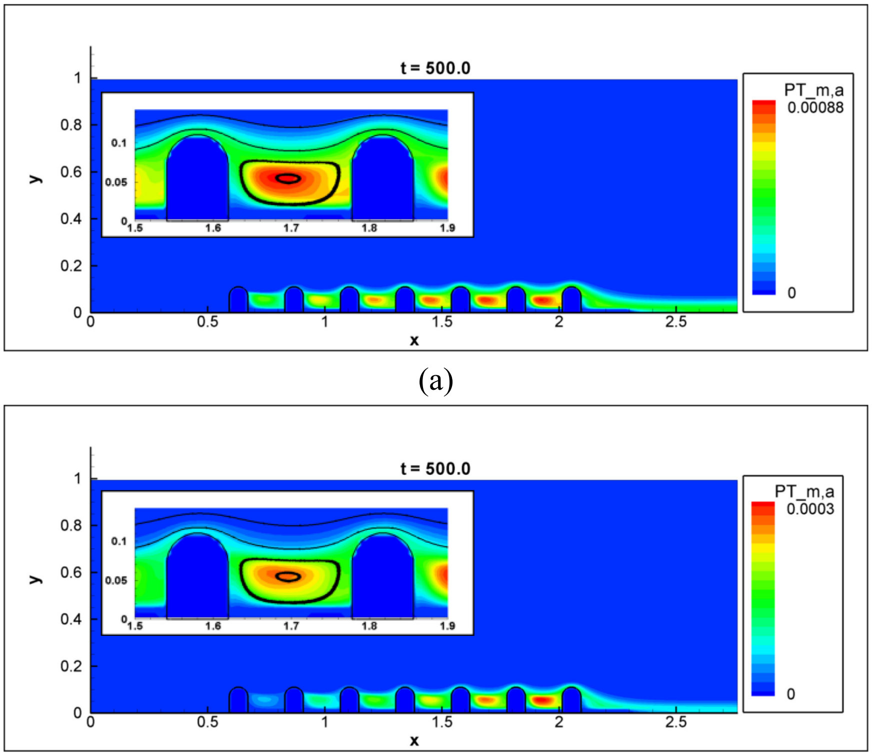

(a)

(b)

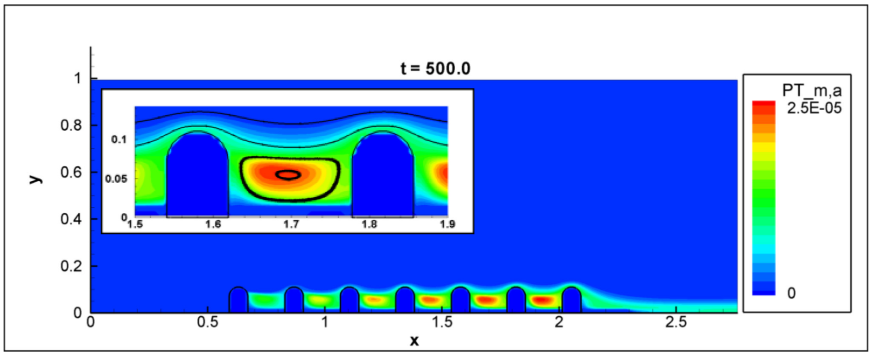

(c)

**Figure 22:** Mobile, activated platelet contours for (a) bare metal stent, (b) flow-delivered AT:H, and (c) DES-delivered AT:H at time $t = 500.0$ for steady flow. The insets are zoomed on the region between struts 5 and 6, and include streamlines for comparison.

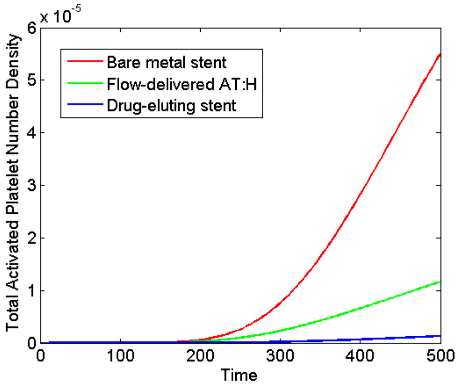

**Figure 23:** Plot of total mobile, activated platelet number density in the domain over time for bare metal stent, flow-delivered AT:H, and DES-delivered AT:H for steady flow.

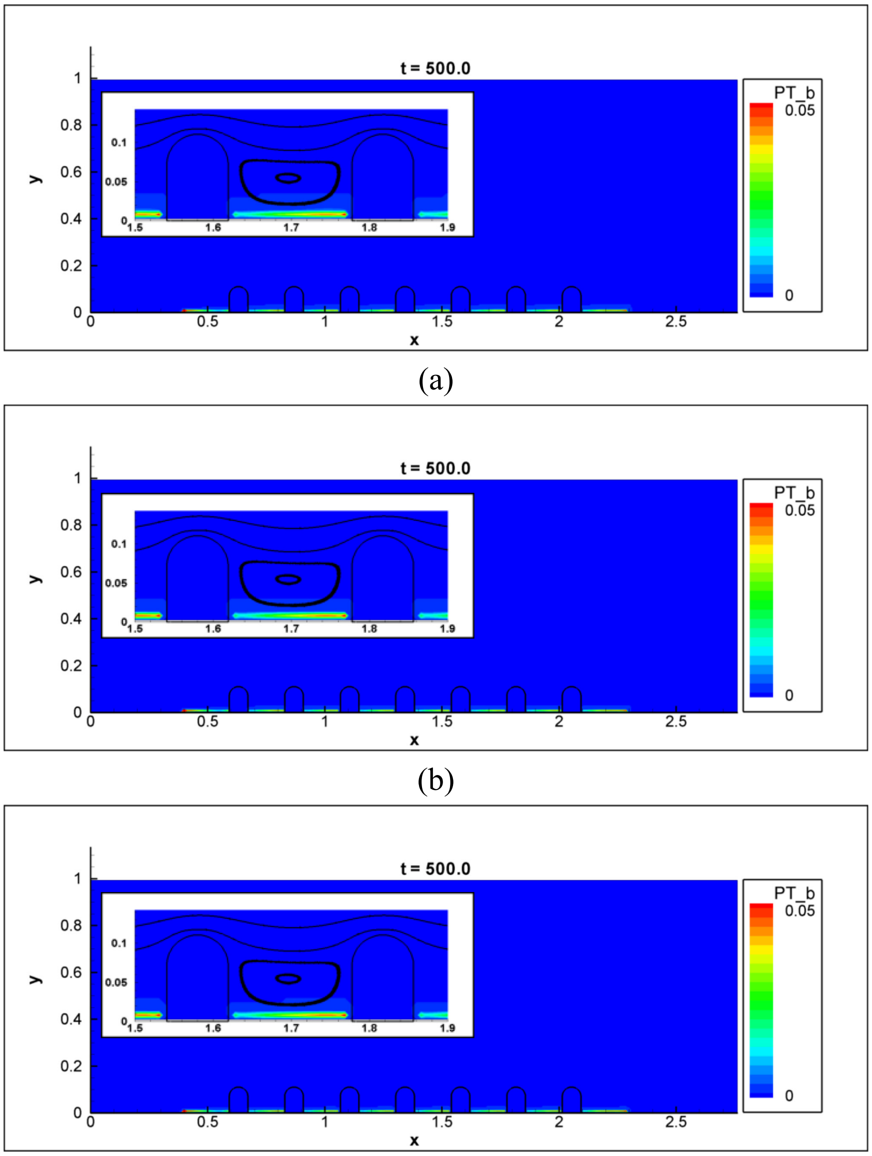

(a)

(b)

(c)

**Figure 24:** Bound platelet contours for (a) bare metal stent, (b) flow-delivered AT:H, and (c) DES-delivered AT:H at time $t = 500.0$ for steady flow. The insets are zoomed on the region between struts 5 and 6, and include streamlines for comparison.

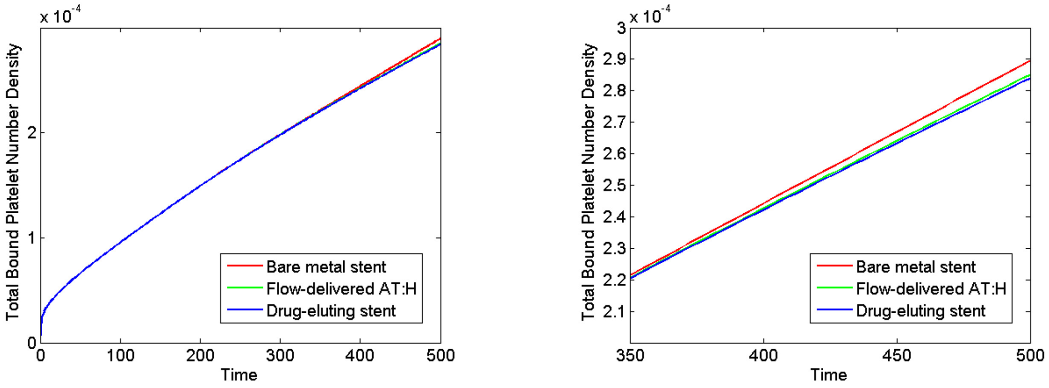

(a) (b)

**Figure 25:** (a) Plot of total bound platelet number density in the domain over time for bare metal stent, flow-delivered AT:H, and DES-delivered AT:H for steady flow. (b) The same plot zoomed in on the late time region.

The mobile, activated platelet contours in figure 22 show similar trends as the thrombin. In all cases the activated platelet number density is highest in the recirculation zones between stent struts, with greater concentrations further downstream. The concentration magnitudes are again very different between the three cases. The total mobile, activated platelet number densities are shown in figure 23, and these also follow the same trend as the thrombin concentrations in figure 21. The DES-delivered anticoagulant is more effective in reducing the amount of platelet activation.

Figure 24 shows bound platelet contours, which includes platelets that have either adhered to the endothelium wall or to other bound platelets. While these contours look almost identical between the three cases, the plots of total number densities in figure 25 do show a small difference from anticoagulant delivery. While the effect is much less pronounced, the anticoagulant does decrease bound platelet number density, with the drug-eluting stent being more effective than the AT:H delivered through the flow. The reason this effect is less pronounced is because in this model bound platelet species can only be produced in close proximity to the wall through adhesion and aggregation processes. This condition severely limits the amount of available activated platelets that can be converted to bound platelets, so the concentration of bound platelets grows much more slowly than that of activated platelets.

### 3.2.2 Pulsatile Flow

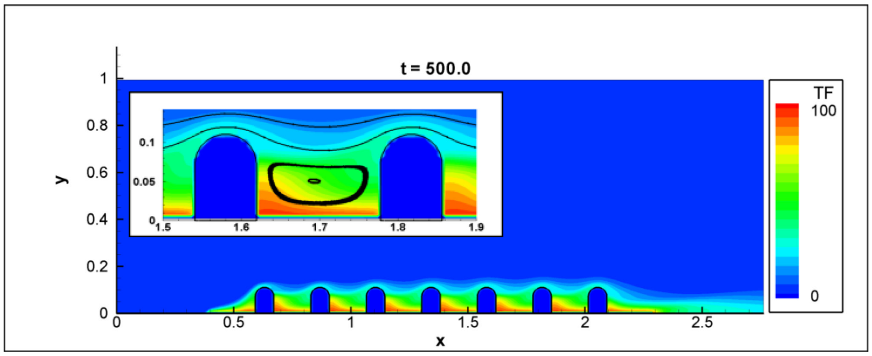

**Figure 26:** Tissue factor contours at time $t = 500.0$ for pulsatile flow. The inset is zoomed on the region between struts 5 and 6, and includes streamlines for comparison.

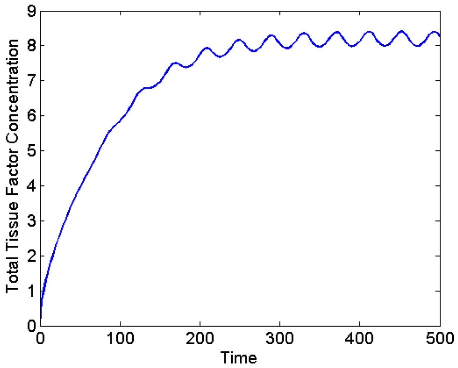

**Figure 27:** Plot of total tissue factor concentration in the domain over time for pulsatile flow.

The pulsatile flow results in general show the same trends as those for steady flow. Figure 26 shows the tissue factor contours at time 500.0, which look very similar to those seen in figure 17 for steady flow. Figure 27 plots the total tissue factor concentration in the domain over time. It is similar to figure 16 for steady flow, but the concentration has minor fluctuations due to advection being driven by a pulsatile flow instead of a steady one.

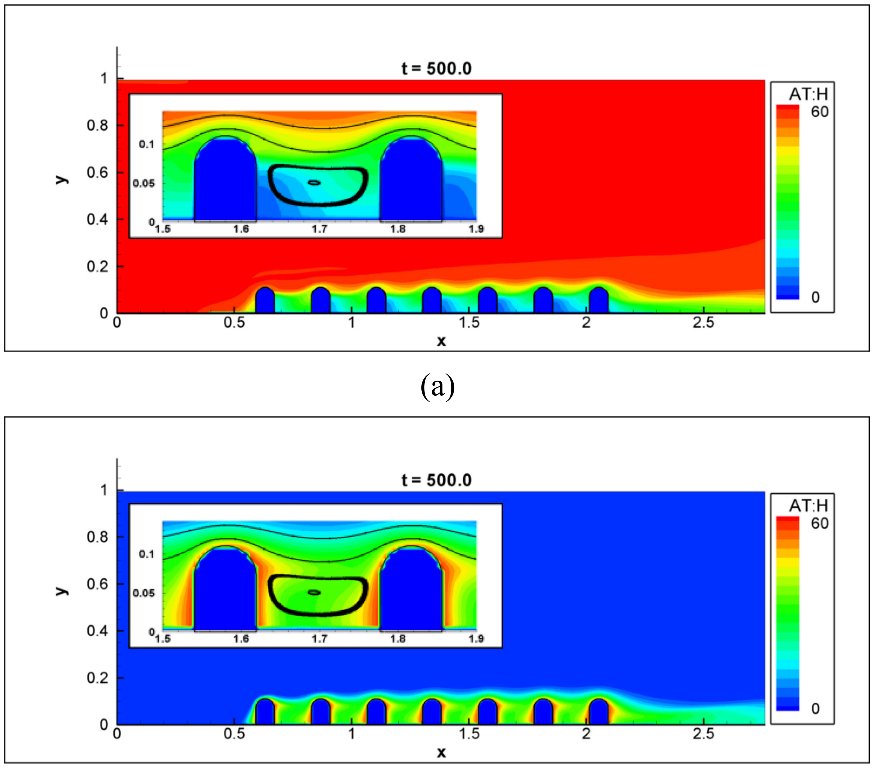

(a)

(b)

**Figure 28:** AT:H contours for (a) flow-delivered AT:H, and (b) drug-eluting stent-delivered AT:H at time $t = 500.0$ for pulsatile flow. The insets are zoomed on the region between struts 5 and 6, and include streamlines for comparison.

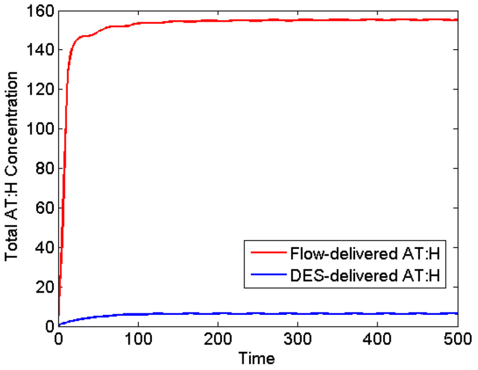

**Figure 29:** Plot of total AT:H concentration in the domain over time for pulsatile flow.

Figure 28 shows the AT:H complex contours at time 500.0 for both flow-delivered and DES-delivered anticoagulant. Figure 29 shows the total concentration of AT:H in the domain for the pulsatile flow. These figures in general show the same results as the steady flow, and the effect of pulsatility on heparin concentration appears to be a minor fluctuation that is added to the dominating heparin concentration trends seen in the steady case. The drug-eluting stent is more effective at delivering anticoagulant into the recirculation zones between stents than the flow.

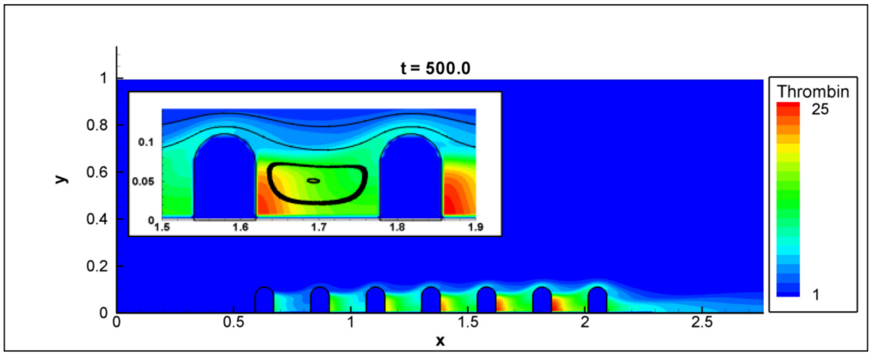

(a)

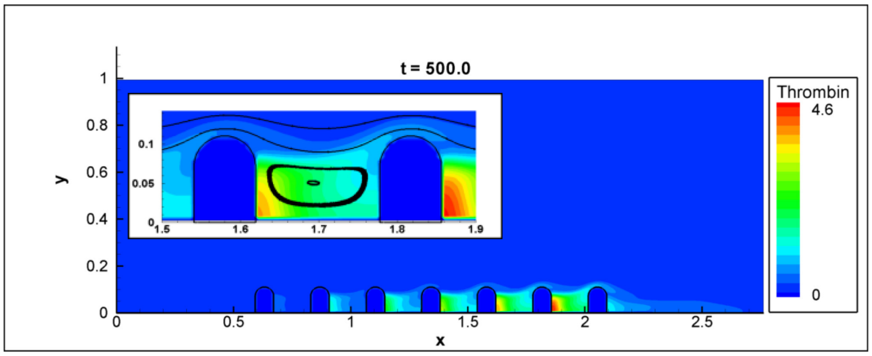

(b)

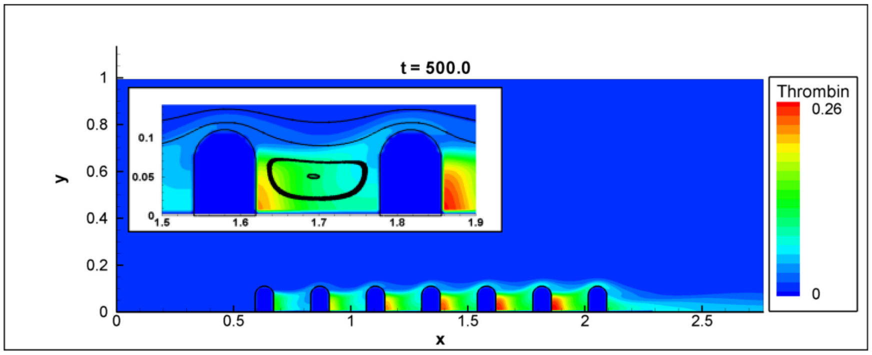

(c)

**Figure 30:** Thrombin contours for (a) bare metal stent, (b) flow-delivered AT:H, and (c) DES-delivered AT:H at time $t = 500.0$ for pulsatile flow. The insets are zoomed on the region between struts 5 and 6, and include streamlines for comparison.

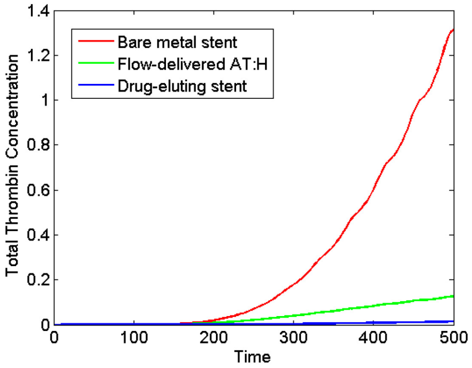

**Figure 31:** Plot of total thrombin concentration over time in the domain for bare metal stent, flow-delivered AT:H, and DES-delivered AT:H for pulsatile flow.

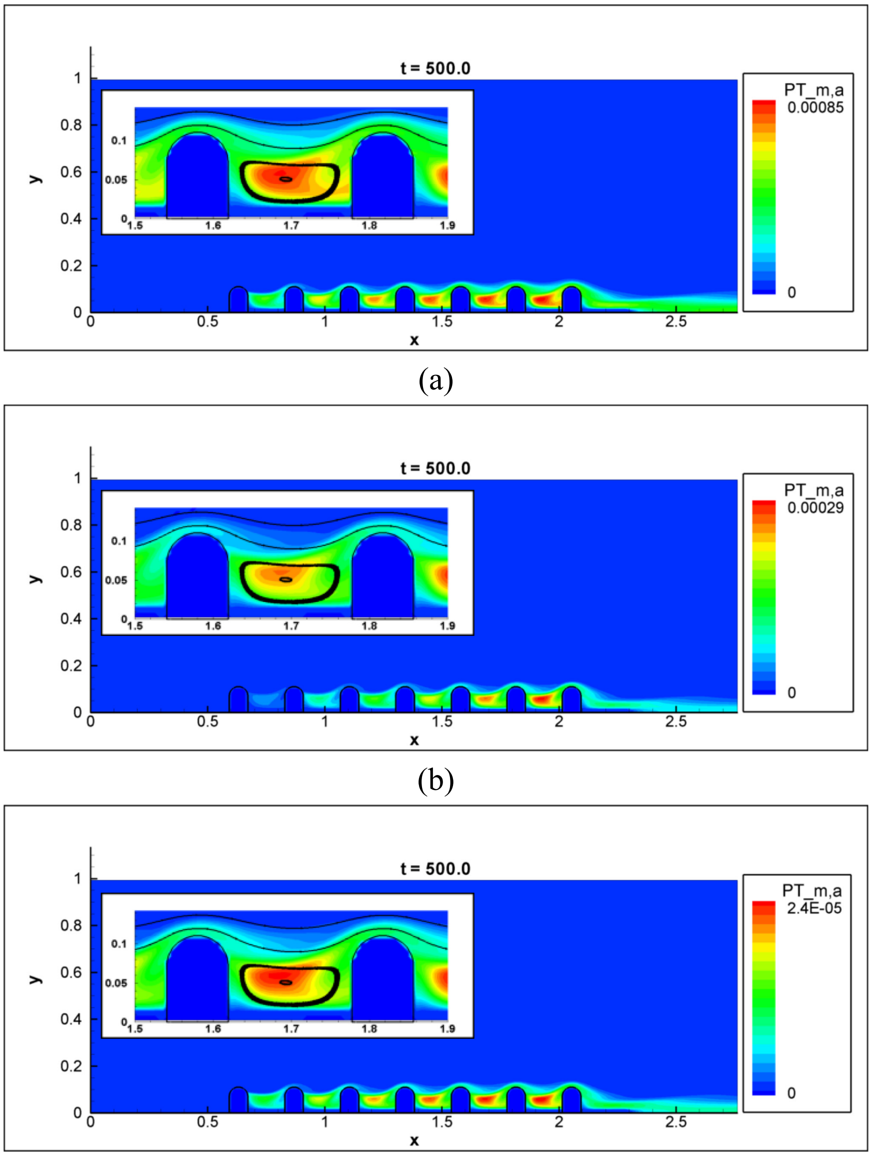

(a)

(b)

(c)

**Figure 32:** Mobile, activated platelet contours for (a) bare metal stent, (b) flow-delivered AT:H, and (c) DES-delivered AT:H at time $t = 500.0$ for pulsatile flow. The insets are zoomed on the region between struts 5 and 6, and include streamlines for comparison.

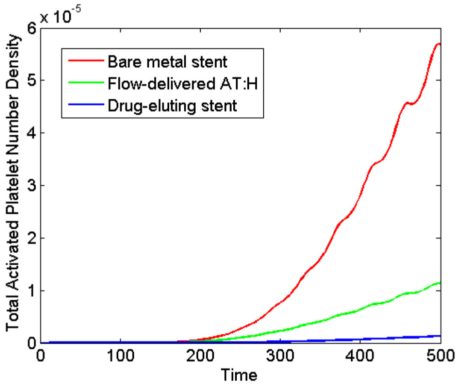

**Figure 33:** Plot of total mobile, activated platelet number density in the domain over time for bare metal stent, flow-delivered AT:H, and DES-delivered AT:H for pulsatile flow.

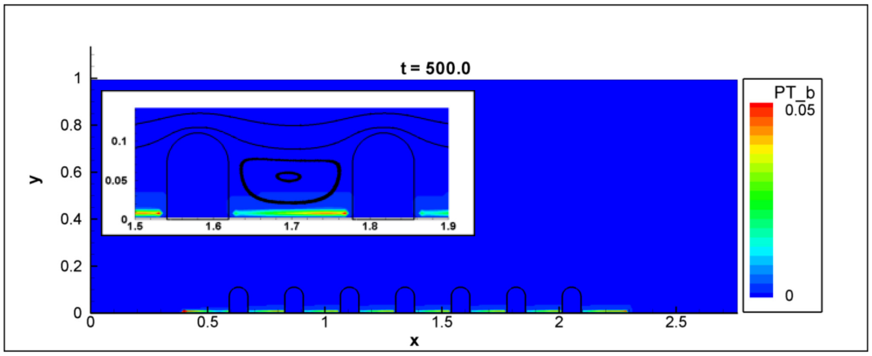

(a)

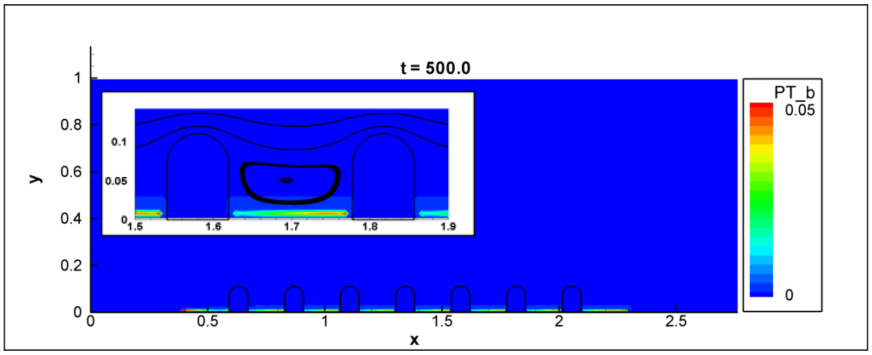

(b)

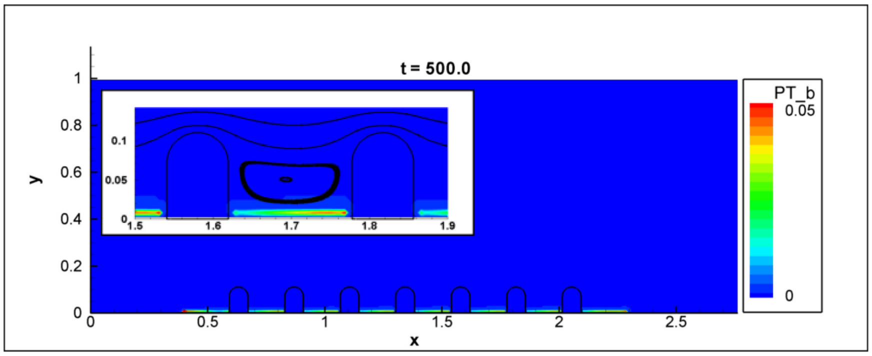

(c)

**Figure 34:** Bound platelet contours for (a) bare metal stent, (b) flow-delivered AT:H, and (c) DES-delivered AT:H at time $t = 500.0$ for pulsatile flow. The insets are zoomed on the region between struts 5 and 6, and include streamlines for comparison.

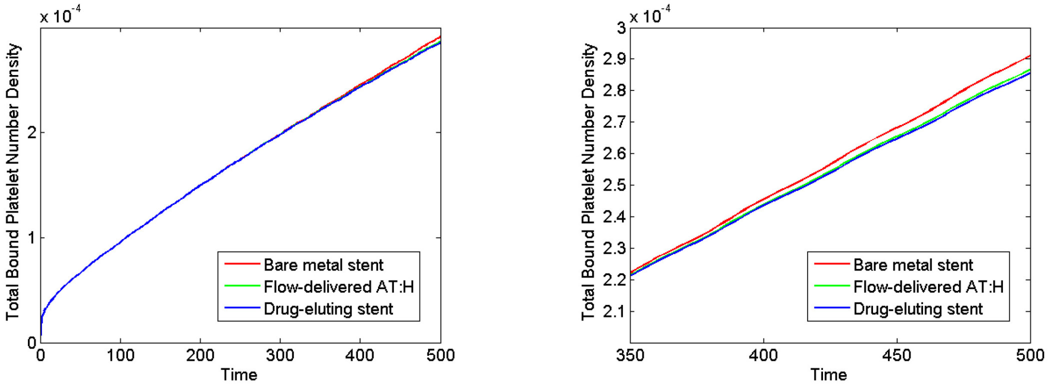

(a) (b)

**Figure 35:** (a) Plot of total bound platelet number density in the domain over time for bare metal stent, flow-delivered AT:H, and DES-delivered AT:H for pulsatile flow. (b) The same plot zoomed in on the late time region.

Figure 30, figure 32, and figure 34 show the contours of thrombin, mobile activated platelets, and bound platelets respectively throughout the domain at time 500.0. The plots of concentration over time of these species are shown in figure 31, figure 33, and figure 35. In general the same trends are observed that were present for steady input flow. The anticoagulant is very effective in reducing the concentrations of thrombin and mobile, activated platelets, with the drug-eluting stent having a significantly larger effect. The bound platelet plots demonstrate the same trend, but with a much smaller difference between the cases because the production of bound platelets requires proximity to the wall.

# 4 Conclusions

This study presents an investigation of stent thrombosis using computational fluid dynamics with coupled scalar transport modeling. The flow properties inside a stented channel were simulated for a curved, complex geometry, and chemical species transport and reaction in the coagulation cascade and platelet interactions were also modeled successfully. The two-dimensional simulation was able to deal with both steady input flows and pulsatile flows such as those in actual blood flow. Overall, the study demonstrated that the chosen methods of numerical modeling are effective in handling the problem of stent thrombosis.

The results of the study showed that antithrombin-heparin complex was an effective anticoagulant for a stented channel after angioplasty. For both steady and pulsatile parabolic inflow, the delivery of heparin significantly reduced the production of thrombin and activation of platelets. The results also showed the effectiveness of drug-eluting stents as a delivery mechanism for anticoagulant AT:H. In all cases, the drug-eluting stent outperformed the flow-delivered anticoagulant as a means of reducing the concentration of thrombin, activated platelets, and bound platelets, which are all highly related to the formation of a blood clot. Furthermore, the amount of anticoagulant released into the domain was orders of magnitude smaller for the drug-eluting stents, and more AT:H remained localized to the area of injury instead of being convected downstream. As the unwanted effects of anticoagulants include bleeding disorders and other medical complications, the benefit of using a lower dose of anticoagulant and having it remain in the region of interest is substantial.

# 5 Future Work

This report represents a preliminary investigation and as such there are various limitations on the scope of this work. The model was entirely two-dimensional and did not reflect real blood vessel or stent shapes. An extension to three dimensions with proper geometry for the wires of the stent could yield different flow properties and chemical transport results. The lengths of the inflow and outflow regions may have an impact on the results, which was not tested thoroughly in this study. Also, the input flow used was a periodic parabolic profile. However, real blood flow in the coronary artery is closer to a Womersley profile created by a fluctuating pressure drop through the artery. Future efforts could implement either a Womersley profile or a fluctuating pressure drop as the boundary conditions at the inflow and outflow. The expression of tissue factor on the injured wall was also greatly simplified in this study. Additionally, the formation of a thrombus requires interactions between activated platelets and fibrin, which was not modeled here. Also each species was assumed to be advected by the flow without affecting it, i.e. massless particles. Accounting for particle masses and their interactions with the flow could lead to differences in the flow properties and transport of chemical species observed. Some of these simplifications can be removed in future work in this area.

# Works Cited

[1] M. Anand, K. Rajagopal, and K. R. Rajagopal, "A Model Incorporating some of the Mechanical and Biochemical Factors Underlying Clot Formation and Dissolution in Flowing Blood," *Journal of Theoretical Medicine*, vol. 5, pp. 183–218, 2003.

[2] Richard W Asinger, Frank L Mikell, Joseph Elsperger, and Morrison Hodges, "Incidence of left-ventricular thrombosis after acute transmural myocardial infarction: serial evaluation by two-dimensional echocardiography," *The New England Journal of Medicine*, vol. 305, no. 6, pp. 297-302, 1981.

[3] Joel L. Berry, Aland Santamarina, James E. Moore Jr., Suranjan Roychowdhury, and William D. Routh, "Experimental and Computational Flow Evaluation of Coronary Stents," *Annals of Biomedical Engineering*, vol. 28, pp. 386–98, 2000.

[4] Jacopo Biasetti, Pier Giorgio Spazzini, Jesper Swedenborg, and T Christian Gasser, "An integrated fluid-chemical model toward modeling the formation of intra-luminal thrombus in abdominal aortic aneurysms," *Frontiers in Physiology*, vol. 3, 2012.

[5] Amy L. Cilia la Corte, Helen Philippou, and Robert A. S. Ariens, "Role of fibrin structure in thrombosis and vascular disease," *Advances in Protein Chemistry and Structural Biology*, vol. 83, pp. 75-127, 2011.

[6] Stéphane Cook and Stephan Windecker, "Early Stent Thrombosis: Past, Present, and Future," *Circulation*, vol. 119, pp. 657-59, 2009.

[7] B T Cooper, G D Long, L C Knight, and K B Manning, "A Novel Approach to the Correlation of Fluid Dynamics and Thromboembolism Associated with Cardiovascular Prosthetic Devices," in *World Congress on Medical Physics and Biomedical Engineering*, Munich, 2009.

[8] Giovanni Davi and Carlo Patrono, "Platelet Activation and Atherothrombosis," *The New England Journal of Medicine*, vol. 357, pp. 2482-94, 2007.

[9] Thomas Q. Dinh, Robert S. Schwartz, and Ronald J. Tuch, "Drug eluting stent," Grant US5697967 A, December 16, 1997.

[10] N Filipovic et al., "Interactions of blood cell constituents: Experimental investigation and computational modeling by discrete particle dynamics algorithm," *Microvascular Research*, vol. 75, pp. 279–284, 2008.

[11] Aaron L Fogelson and Robert D Guy, "Immersed-boundary-type models of intravascular platelet aggregation," *Computer Methods in Applied Mechanics and Engineering*, vol. 197, pp. 2087–2104, 2008.

[12] Aaron L Fogelson, Yasmeen H Hussain, and Leiderman Karin, "Blood Clot Formation under Flow: The Importance of Factor XI Depends Strongly on Platelet Count," *Biophysical Journal*, vol. 102, pp. 10-18, 2012.

[13] Bruce Furie and Barbara C Furie, "Mechanisms of Thrombus Formation," *The New England Journal of Medicine*, vol. 359, pp. 938-949, 2008.

[14] Laurie J Gay and Brunhilde Felding-Habermann, "Contribution of platelets to tumour metastasis," *Nature Reviews Cancer*, vol. 11, no. 2, pp. 123-134, 2011.

[15] Robert D Guy and Aaron L Fogelson, "Probabilistic Modeling of Platelet Aggregation: Effects of Activation Time and Receptor Occupancy," *Journal of Theoretical Biology*, vol. 219, pp. 33-53, 2002.

[16] S E Harrison, S M Smith, J Bernsdorf, D R Hose, and P V Lawford, "Application and validation of the lattice Boltzmann method for modelling flow-related clotting," *Journal of Biomechanics*, vol. 40, pp. 3023–3028, 2007.

[17] Javaid Iqbal, Julian Gunn, and Patrick W. Seeuys, "Coronary stents: historical development, current status and future directions," *British Medical Bulletin*, pp. 1-19, 2013.

[18] Hiroki Kamada et al., "A three-dimensional particle simulation of the formation and collapse of a primary thrombus," *International Journal for Numerical Methods in Biomedical Engineering*, vol. 26, pp. 488-500, 2010.

[19] S Kamath, A D Blann, and G Y H Lip, "Platelet activation: assessment and quantification," *European Heart Journal*, vol. 22, pp. 1561–1571, 2001.

[20] Dimitrios E. Kiousis, T. Christian Gasser, and Gerhard A. Holzapfel, "A Numerical Model to Study the Interaction of Vascular Stents with Human Atherosclerotic Lesions," *Annals of Biomedical Engineering*, vol. 35, no. 11, pp. 1857–69, 2007.

[21] Michael H Kroll and Vahid Afshar-Kharghan, "Platelets in pulmonary vascular physiology and pathology," *Pulmonary Circulation*, vol. 2, no. 3, pp. 291-308, 2012.

[22] Karin Leiderman and Aaron L Fogelson, "Grow with the flow: a spatial–temporal model of platelet deposition and blood coagulation under flow," *Mathematical Medicine and Biology*, vol. 28, pp. 47-84, 2011.

[23] Peter Libby and Daniel I. Simon, "Inflammation and Thrombosis: The Clot Thickens," *Circulation*, vol. 103, pp. 1718-20, 2001.

[24] P Worth Longest and Clement Kleinstreuer, "Comparison of blood particle deposition models for non-parallel flow domains," *Journal of Biomechanics*, vol. 36, pp. 421-430, 2003.

[25] Catherine Loudon and Antoinette Tordesillas, "The Use of the Dimensionless Womersley Number to Characterize the Unsteady Nature of Internal Flow," *Journal of Theoretical Biology*, vol. 191, pp. 63-78, 1998.

[26] R. Mittal et al., "A versatile sharp interface immersed boundary method for incompressible flows with complex boundaries," *Journal of Computational Physics*, vol. 227, pp. 4825–52, 2008.

[27] Rajat Mittal and Gianluca Iaccarino, "Immersed Boundary Methods," *Annual Review of Fluid Mechanics*, vol. 37, pp. 239–61, 2005.

[28] Daisuke Mori et al., "Simulation of platelet adhesion and aggregation regulated by fibrinogen and von Willebrand factor," *Thrombosis and Haemostasis*, vol. 99, pp. 108–115, 2008.

[29] Andrew Narracott et al., "Development and validation of models for the investigation of blood clotting in idealized stenoses and cerebral aneurysms," *Journal of Artificial Organs*, no. 8, pp. 56–62, 2005.

[30] A N Neskovic, J Marinkovic, M Bojic, and A D Popovic, "Predictors of left ventricular thrombus formation and disappearance after anterior wall myocardial infarction," *European Heart Journal*, vol. 19, pp. 908-916, 1998.

[31] Giuseppe Pontrelli and Filippo de Monte, "A multi-layer porous wall model for coronary drug-eluting stents," *International Journal of Heat and Mass Transfer*, vol. 53, pp. 3629–37, 2010.

[32] V L Rayz et al., "Flow Residence Time and Regions of Intraluminal Thrombus Deposition in Intracranial Aneurysms," *Annals of Biomedical Engineering*, vol. 38, no. 10, pp. 3058–3069, 2010.

[33] Zaverio M Ruggeri and G Loredana Mendolicchio, "Adhesion Mechanisms in Platelet Function," *Circulation Research*, vol. 100, pp. 1673-1685, 2007.

[34] Dmitri V. Sakharov, Leonid V. Kalachev, and Dingeman C. Rijken, "Numerical Simulation of Local Pharmacokinetics of a Drug after Intravascular Delivery with an Eluting Stent," *Journal of Drug Targeting*, vol. 10, no. 6, pp. 507–13, 2002.

[35] Erik N Sorensen, Greg W Burgreen, William R Wagner, and James F Antaki, "Computational Simulation of Platelet Deposition and Activation: I. Model Development and Properties," *Annals of Biomedical Engineering,* vol. 27, pp. 436–448, 1999.

[36] Erik N Sorensen, Greg W Burgreen, William R Wagner, and James F Antaki, "Computational Simulation of Platelet Deposition and Activation: II. Results for Poiseuille Flow over Collagen," *Annals of Biomedical Engineering*, vol. 27, pp. 449–458, 1999.

[37] Masaaki Tamagawa, Hiroaki Kaneda, Miki Hiramoto, and Sho Nagahama, "Simulation of Thrombus Formation in Shear Flows Using Lattice Boltzmann Method," *Artificial Organs*, vol. 33, no. 8, pp. 604-610, 2009.

[38] Giuseppe Vairo, Margherita Cioffi, Riccardo Cottone, Gabriele Dubini, and Francesco Migliavacca, "Drug release from coronary eluting stents: A multidomain approach," *Journal of Biomechanics*, vol. 43, pp. 1580–89, 2010.

[39] J M van Dantzig, B J Delemarre, H Bot, and C A Visser, "Left ventricular thrombus in acute myocardial infarction," *European Heart Journal*, vol. 17, pp. 1640-1645, 1996.

[40] Stephan Windecker and Bernhard Meier, "Late Coronary Stent Thrombosis," *Circulation*, vol. 116, pp. 1952-65, 2007.

[41] T. Cooper Woods and Andrew R. Marks, "Drug-Eluting Stents," *Annual Review of Medicine*, vol. 55, pp. 169–78, 2004.

[42] David M Wootton, Christos P Markou, Stephen R Hanson, and David N Ku, "A Mechanistic Model of Acute Platelet Accumulation in Thrombogenic Stenoses,"

*Annals of Biomedical Engineering*, vol. 29, pp. 321-329, 2001.

[43] Zhiliang Xu, Nan Chen, Malgorzata M Kamocka, Elliot D Rosen, and Mark Alber, "A multiscale model of thrombus development," *Journal of the Royal Society Interface*, vol. 5, pp. 705-722, 2008.

[44] Zhiliang Xu, Oleg Kim, Malgorzata Kamocka, Elliot D Rosen, and Mark Alber, "Multiscale models of thrombogenesis," *WIREs Systems Biology and Medicine*, vol. 4, pp. 237-246, 2012.

[45] Houman Zahedmanesh, Daniel John Kelly, and Caitriona Lally, "Simulation of a balloon expandable stent in a realistic coronary artery—Determination of the optimum modelling strategy," *Journal of Biomechanics*, no. 43, pp. 2126–32, 2010.

[46] P. Zunino et al., "Numerical simulation of drug eluting coronary stents: Mechanics, fluid dynamics and drug release," *Computer Methods in Applied Mechanics and Engineering*, no. 198, pp. 3633–44, 2009.

# Curriculum Vitae

## Personal

- Born September 26, 1990 in Tuscaloosa, AL, USA

## Education

- M.S.E. in Mechanical Engineering, Johns Hopkins University, 2014
- B.S. in Applied Physics, California Institute of Technology, 2012

## Research and Professional Experience

- **Graduate Research for Masters Thesis**  
  *Jun 2012 – present*  
  Mechanical Engineering, Johns Hopkins University

  Developed and applied computational models of thrombus formation in various blood flow environments with recirculating flow. The models included the reaction cascade for platelet activation and interactions between activated platelets.

- **ORISE Student Research Participation Program**  
  *Jun. - Aug. 2013*  
  JHU Applied Physics Laboratory (APL)

  Modeled laser-induced thermal damage both theoretically and numerically. The multiphysics problem combined heat transfer, fluid mechanics, optics, and gas dynamics.

- **Teaching Assistant**
  *Aug. - Dec. 2012*
  Mechanical Engineering, Johns Hopkins University

  Taught a freshman laboratory in mechanical engineering that covered experiments in fundamental mechanics with analysis in MATLAB. (8 hrs/ week)

- **Summer Undergraduate Research Fellowship (SURF) Student**
  *Jun. - Sep. 2011*
  Chemical Engineering, California Institute of Technology

  Utilized the Brownian dynamics method to develop a model and computer code for simulating motion of diffusiophoretic osmotic motor particles in a colloidal dispersion exhibiting a reactant gradient, and evaluated the translational and angular displacements over time.

- **Summer Undergraduate Research Fellowship (SURF) Student**
  *Jun. - Sep. 2010*
  Aerospace Engineering, California Institute of Technology

  Performed particle image velocimetry experiments on superhydrophobic carbon nanotubes in a water tunnel, and analyzed the quantitative effects on surface drag and boundary layer properties.

- **Summer Student Research Assistant**
  *Jun. - Sep. 2009*
  Wright Center of Innovation, The Ohio State University

  Performed imaging analysis on medical samples using micro-CT, PET, and MRI.

## Publications

1. Ghosh and K. A. Iyer. Theoretical and numerical modeling approaches for high-energy laser-induced thermal damage. Journal of Applied Physics Reviews (2013). To be submitted.

2. J. Johnson, A. Ghosh, and J.J. Lannutti. Microstructure-property relationships in a tissue-engineering scaffold. Journal of Applied Polymer Science, Vol. 104 No. 5 p. 2919-27 (2007).

## Conference Papers

1. Aria, C. Shu, A. Ghosh, and M. Gharib. Dynamics of water droplet on a superhydrophobic carbon nanotube array. Presented at the 63rd Annual Meeting of the APS Division of Fluid Dynamics, Vol. 55, No. 16, Long Beach, CA (2010).
2. Rath, R. Perera, J. Deschner, P. Ahuja, A. Ghosh, and S. Agarwal. Passive Motion and Immobilization both induce Proinflammatory Genes in Grade Three osteoarthritic Cartilage, but Passive Motion protects low Grade osteoarthritic Cartilage Damage. Presented at the 54th Annual Meeting of the Orthopedic Research Society, San Francisco, CA (2008).

## Presentations

1. Ghosh. Interactions of High-Energy Lasers with Metals. Johns Hopkins University, Sep 2013.
2. Ghosh. Laser Interactions with Metals: Summer in Review. JHU Applied Physics Laboratory (APL) Space Research Department, Aug 2013.
3. Ghosh. Effect of globally imposed reactant gradients on osmotic propulsion, SURF Seminar Day, California Institute of Technology, Oct 2011.
4. Ghosh. Drag reduction using superhydrophobic carbon nanotube arrays, SURF Seminar Day, California Institute of Technology, Oct 2010.

## .Awards and Honors

- **Oak Ridge Institute for Science and Education Summer Fellow**
  Oak Ridge Institute for Science and Education (ORISE), *2013*
- **Summer Undergraduate Research Fellowship (SURF)**
  California Institute of Technology , *2011*

- **Summer Undergraduate Research Fellowship (SURF)**
  California Institute of Technology , *2010*

- **National AP Scholar Award**
  College Board AP, *2008*

- **National Merit Scholarship Finalist**
  National Merit Scholarship Corporation, *2008*

## Technical Skills

- **Programming Languages:** Proficient in FORTRAN 90/95, Python, MATLAB, Latex, Java, Perl, C++

- **Software:** Proficient in Mathematica, COMSOL, TecPlot 360, PIVview, POV-ray, Solidworks

- Fabrication skills from carbon nanotube labs and solid-state electronics labs (includes chemical vapor deposition (CVD), photolithography, etching, doping)

- Particle image velocimetry (PIV) in a water tunnel and high-speed camera use

- Circuit design and use of oscilloscope

- 3D scanner and associated software